Studies on

High-*k* Gate Stacks

by

High-resolution Rutherford Backscattering Spectroscopy

Dissertation

Ming ZHAO

2008

DEPARTMENT OF MICRO ENGINEERING
KYOTO UNIVERSITY
KYOTO, JAPAN

Acknowledgements

First, I would like to express my sincere gratitude to Prof. Kenji Kimura, who spends a lot of time and spirit on teaching me, training me, discussing with me, and doing experiments with me. It was very lucky of me to meet such a nice person and convince him to be my dissertation supervisor. When ever I asked for a help, he always grants me a favor. I want to thank him for all the patient guidance, constructive suggestions, and warm encouragements throughout these years.

I would also like to thank Prof. Kouichi Ono and Prof. Akitomo Tachibana of Kyoto University for their critical suggestions and reading.

I am further deeply indebted to Dr. Kaoru Nakajima, who accompanied me in uncountable number of experiments, guided me in interpreting the results, encouraged me in the difficult time, and always had a helping hand no matter how busy he was himself.

I am also grateful to Prof. Motofumi Suzuki for his fruitful comments and warm encouragements through this study. I would also like to express the gratitude to Dr. Kazuyoshi Torii, who prepared the high-*k* stack samples many times for me. I am also very grateful to Mr. Kinoshita for his kind advices and help on AFM and SEM. I am very grateful to Prof. Masashi Uematsu, Dr. Satoshi Kamiyama, Dr. Yasuo Nara, and Prof. Keisaku Yamada for their great comments and kind help.

I am also very appreciative of my colleges in Kimura lab, Mr. Matsushita who has been my tutor and helped me to be familiar with the environment here, Mr. Hosoi who accompanied me during many experiments, and Mr. Fujiyoshi for preparing the auto controllable goniometer setup.

At the end, I want to extend my sincerely thanks to all the people who contribute to this work, to the members of the Department of Micro Engineering of Kyoto University, to my family and friends, to many people I met here who made this three years to be a good memory of Japan.

Kyoto

January, 2008 **Ming Zhao**

CONTENTS

1. Introduction 1

1.1 The high-*k* dielectrics 2

1.2 Requirements for high-*k* dielectrics 2

1.3 Investigation of high-*k* dielectrics 3

1.4 Challenge of high-*k* dielectrics 4

1.5 Challenge of high-*k* dielectrics measurement 5

1.6 Outline of this thesis 6

Reference 7

2. Experiments 11

2.1 Fundamentals of RBS 12

2.2 Setup of HRBS system with a magnetic spectrometer 17

2.3 Thermal treatment systems 19

2.4 Preparation of $HfO_2/SiO_2/Si$ stacks 20

2.5 Setup of RBS with Time-of-Flight (TOF) system 20

References 26

3. Si emission from the SiO_2/Si interface during the growth of SiO_2 in the $HfO_2/SiO_2/Si$ structure 29

3.1 Introduction 30

3.2 Experimental 31

3.3 Results and discussion 31

3.3.1 Characteristic of as-grown sample-1 by HRBS 31

3.3.2 Si outward emission during the interface SiO_2 growth 34

3.3.3 Temperature dependence of the Si emission 38

3.3.4 Annealing time dependence of the Si emission 38

3.4 Conclusions 41

References.....41

4. Isotopic labeling study of the oxygen diffusion in $HfO_2/SiO_2/Si$ 43

4.1 Introduction.....44

4.2 Experimental.....45

4.3 Results and discussion 45

4.3.1 Growth of the interfacial SiO_2.....45

4.3.2 Isotopic tracing.....48

4.3.3 Temperature dependence of the growth rate of the interfacial SiO_2 layer 51

4.3.4 Estimation of concentration of oxygen interstitial 53

4.4 Conclusions.....54

References.....54

5. In situ observation of oxygen gettering by titanium overlayer on $HfO_2/SiO_2/Si$ using high-resolution Rutherford backscattering spectroscopy 57

5.1 Introduction.....58

5.2 Experimental.....58

5.3 Results and discussion 59

5.3.1 Oxygen getting by Ti deposition 59

5.3.2 The thickness of Ti layer influence on the oxygen getting amount.....62

5.4 Conclusions.....65

5.5 Acknowledgement 65

References.....65

6. The development of the Time-of-flight RBS 67

6.1 Introduction.....68

6.2 Experimental.....69

6.2.1 Equipments.....69

6.2.2 Estimation of the width of the pulsed beam.....69

6.2.3 Derivation of the depth information.....72

6.3 Results 74
6.3.1 Determination of t_0 74
6.3.2 The energy spectra and depth profiles 74
6.3.3 Observation of the blocking pattern 76
6.3.4 Depth dependence of the blocking pattern 80
6.4 Conclusions 80
Reference 82

Chapter 1

Introduction

Abstract

This thesis is on the study of the characterization of interfaces and surfaces of high-*k* stacks for the future microelectronics. The changes of the high-*k* stacks during thermal processing and its mechanism have been experimentally investigated by high-resolution Rutherford Backscattering Spectrometry (HRBS) in combination with isotope tracing. The experimental results are consistent with the theoretical prediction that the silicon will be emitted outward to release the stress which is induced by the interface Si oxidation. Then, we studied the potential method, oxygen-gettering by Ti overlayer, for controlling the interface SiO_2 thickness. Furthermore, we proposed a Time-Of-Flight (TOF) detector system for application on crystallographic analysis. TOF-RBS system is capable to analyze the sample's crystallographic and chemical information even at the near surface of the sample, which is strongly required by the future microelectronics industry.

In this chapter, brief introduction to the high-*k* stacks and the outline of this thesis are described.

1.1 The high-*k* dielectrics

Started by the invention of the Si-based metal-oxide-semiconductor field-effect transistor (MOSFET) in 1960 [1,2], the silicon age arose and significantly changed people's lives.

The progress of the Si-based microelectronics industry goes by doubling the number of components per integrated circuit every 12-18 months for the last 40 years. The technological route followed by this industry was to perform a calculated reduction on the dimensions, called "scaling", of the Si-based MOSFET [3].

The key element enabling the scaling of Si MOSFETs is SiO_2 which has been employed to isolate the transistor gate from the Si channel for decades. The use of amorphous, thermally grown SiO_2 as a gate dielectric provides thermodynamically and electrically stable, high-quality Si-SiO_2 interface with superior electrical isolation properties [4, 5]. In fact, the silicon age owes its existence to the superb quality of thermally grown SiO_2 as gate insulator and Si surface electrical passivator. The fundamental device design and the basic materials, SiO_2, have such excellent performance that they have served for 40 years without any question [6].

Nevertheless, the outstanding evolution of the silicon age is rapidly approaching a saturation point where device fabrication can no longer be simply scaled to progressively smaller sizes. The direct tunneling of electrons through the SiO_2 will induce the gate leakage current if the thickness of the SiO_2 layer become too thin (under 1.3 nm) [7]. In addition it becomes increasingly difficult to make and measure accurately such thin films. Finally, the reliability of SiO_2 films against electrical breakdown declines in thin films.

Hence, further development in Si-based integrated circuits will rely on the use of alternative materials with dielectric constants much higher than that of silicon oxide. These so called high-*k* dielectrics, which include a number of transition-metal and rare-earth oxides, silicates, and aluminates deposited on Si, became an extremely active, almost frenetic research area because if they are ever introduced in fabrication technology, that will constitute the first materials revolution in the silicon age [8-15].

1.2 Requirements for high-*k* dielectrics

The requirements of the new high-*k* dielectrics are six-fold.

1. Its dielectric constant (k) must be large enough to be used for a reasonable number of years of scaling, preferably 25-30.

2. The oxide directly contact with the Si channel, so it must be thermodynamically stable with Si.

3. It must be kinetically stable and be compatible to the thermal processing to 1000˚C for 5 s (in present process flows).

4. It must act as an insulator, by having band offset with Si of over 1 eV to minimize carrier injection into its bands.

5. It must form a good electrical interface with Si.

6. The density of electrically active defects must be as small as possible.

Compared to SiO_2, all the other dielectric materials have a worse electrical interface with Si [16, 17]. In order to achieve a better electrical interface with Si, much of the effort toward replacement of SiO_2 has been focused on stack structures, composed of an ultrathin SiO_2 buffer layer underneath the high-k dielectric film. Figure 1-1 provides a schematic view of the various regions associated with the gate stack of a CMOSFET. The largest benefit of using SiO_2 as the lower interface of the stack is that the unparalleled quality of the SiO_2-Si interface will help to maintain a high channel carrier mobility.

This thesis focuses on the changes of the gate dielectric and the high-k/Si interface in the high-k stacks during the thermal process.

1.3 Investigation of high-*k* dielectrics

Many of the materials initially chosen as potential alternative gate dielectric candidates were inspired by memory capacitor applications. However, in a memory capacitor the high-k/Si interface quality is not as critical to capacitor performance as that to transistors. The interface defects between the dielectric materials and the Si substrate failed many of the candidates from this area except for Al_2O_3 [18]. Although, Al_2O_3 has been extensively studied for its many favorable properties, it can only be applied as a short-term solution for industry's needs (1-2 generations) due to its lower k (8-10). Recent years, a substantial amount of investigation has gone into the group IVB metal oxides, specifically TiO_2 [19-21], ZrO_2 [22-24] and HfO_2 [25-27], as these systems have shown much promise in overall materials properties as candidates to replace SiO_2.

TiO_2 has been extensively studied for high-*k* applications because it has high permittivity of *k* = 80-100. However, Ti has several stable oxidation states of Ti^{3+} and Ti^{4+} which lead to a well known problem: a reduced oxide. Such a reduced oxide has many oxygen vacancies which act as carrier traps and high leakage paths.

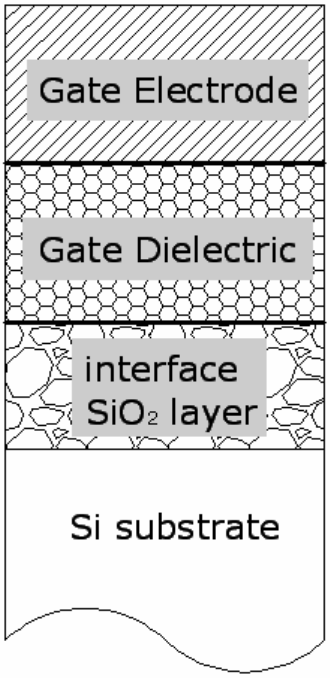

Fig. 1-1 Schematic drawing of important regions of a field effect transistor gate stacks.

According to the requirements for the potential high-*k* materials, ZrO_2 and HfO_2 are the most promising candidates for replacing SiO_2. This is due to their excellent dielectric properties with a typical gate leakage reduction of 10^4-10^6, high permittivity of about 25, good mobility and threshold voltage stability, and thermal stability in contact with silicon. Other requirements on gate dielectric materials like low density of interface states, gate compatibility, structural, physical and chemical stability at both gate electrode/dielectric and dielectric/Si interfaces are currently under intensive investigation as semiconductor manufacturers are anticipating 45 nm channel length devices using high-*k* dielectrics.

This thesis studies on the high-*k* stacks with HfO_2 as the gate dielectric.

1.4 Challenge of high-*k* dielectrics

Integration of high-*k* dielectrics into silicon technology is a challenge. The high-*k* oxides differ from SiO_2 in that their bonding is ionic and they have a higher

coordination number, which means high-*k* oxides are poorer glass formers. As the result of the poor glass-forming ability and high coordination, the oxide network is less able to relax to rebond and remove defects [28, 29].

The oxygen vacancy and oxygen interstitial are the two most likely intrinsic defects in HfO_2 in terms of their formation energies. Since the higher defects density leads to the poor electrical properties, the interface quality of this system remains a critical issue [30, 31].

Therefore, to control the integrity of the gate dielectric in ultra-large scale integration (ULSI) processing it is necessary to gather enough information on the thermal stability of high-*k* dielectrics on Si in oxygen containing atmospheres, from extremely low to rather high O_2 partial pressures, and on the effect of different parameters like temperature, time and partial pressures of the different gaseous components of the annealing atmospheres, as well as interlayer composition and thickness in order to build up an adequate model of the system which is prone to be incorporated to circuit design codes.

1.5 Challenge of high-*k* dielectrics measurement

The interface between high-*k* material and the underlying substrate plays a significant role in determining the overall electrical properties of high-*k* stacks. The ability to determine structural and compositional information from the near-surface region of a semiconductor material is extremely important for the further investigation and development of microelectronics industry. A large array of experimental techniques already exists capable of giving high quality structural and chemical information, although the most widely used techniques for the investigation of semiconductor materials are X-ray diffraction (XRD) for structural analysis and secondary ion mass spectrometry (SIMS) for chemical analysis. However, these techniques have limitations if the layered structure to be investigated is in the near-surface region, i.e. less than few nanometers below the surface of the material. Both of these techniques require a certain thickness of material to be studied. In the case of XRD, the layers should generally occupy some fraction of the extinction distance. And for SIMS, the sputtering process must reach an equilibrium. Also, although a number of other surface analysis techniques are available, e.g. XPS and AES, their penetration distance into a material is limited by the mean free path of the excited electrons and therefore they analyze only the top surface (1-2 nm) of the material.

Rutherford backscattering spectroscopy (RBS) has been in use since the 1960's and become a major materials-characterization method, which is one of the most frequently used techniques to obtain quantitative information of composition, different layer's thickness and depth profile of the near-surface region. The depth resolution of the conventional RBS is ~10 nm [32]. Using a magnetic spectrometer, the depth resolution of RBS was improved up to ~2 nm in tungsten [33]. The development of the position-sensitive-detector system for the spectrometer seriously improved its precision. In the 1990s, a variety of electrostatic and magnetic spectrometers and time-of-flight telescopes were developed for high-resolution RBS (HRBS). The HRBS setup with position sensitive detector (PSD) and the magnetic spectrometer in Kyoto University could achieve the ultimate depth resolution, namely the monolayer resolution [34].

1.6 Outline of this thesis

In this thesis, we investigate the mechanism of the oxygen and silicon diffusion through gate dielectrics, as well as the oxygen and the silicon reaction at the Si channel layer of the high-*k* stack during thermal process for $HfO_2/SiO_2/Si$ stacks by using HRBS. In addition, the development of TOF-RBS system is presented.

Chapter 2 described the experimental methods; preparation of samples, the apparatus and physical basis of HRBS, and the apparatus of the time-of-flight (TOF) RBS system.

In chapter 3, the characteristic change of the $HfO_2/SiO_2/Si$ stack structure during the thermal process in oxygen containing atmospheres was investigated. The growth of the interfacial SiO_2 layer and simultaneous surface accumulation of Si were observed. The correlation of the surface accumulation of Si and the growth of the interfacial SiO_2 was discussed.

In chapter 4, oxygen isotope was used to clarify the oxygen diffusion characteristic in the high-*k* dielectrics during the thermal processing. A diffusion model of oxygen in high-*k* stacks was discussed based on the experimental result. The defects density in the high-*k* dielectric was also estimated from the experimental result.

In chapter 5, titanium was deposited on the $HfO_2/SiO_2/Si$ stacks and the sample was annealed in vacuum. The reduction of interfacial SiO_2 layer and oxygen depletion in high-*k* dielectric layer were observed.

In chapter 6, a time-of-flight (TOF) RBS system having a wide acceptance angle of

±6.85° was developed for crystallographic analysis of thin films. This system was applied to analyze Si(100). Clear blocking patterns were observed. Detailed features of this system are described.

Reference

[1] D. Kahgn, U.S. Patent No. 3,102,230 (27 August 1963).

[2] M. M. Atalla, U.S. Patent No. 3,056,888 (2 October 1962).

[3] D. J. Frank, Proc. IEEE **89,** 259 (2001).

[4] E. P. Gusev, in: G. Pachionni (Ed.), Defects in SiO_2 and Related Dielectrics: Science and Technology, Kluwer Academic Publishers, Dordrecht, 2000, p.1.

[5] M. L Green, E. P Gusev, R. Degraeve, E. L. Garfunkel, Applied physics review, J. Appl. Phys. **90**, 2057(2001).

[6] L.C. Feldman, E. P Gesev, E. Garfunkel, in: E. Garfunkel, E. P. Gusev, A. Vul' (Eds.), Fundamental Aspects of Ultrathin Dielectrics on Si-based Devices, Kluwer Academic Publishers, Dordrecht, 1998, p.1.

[7] S.H. Lo, D.A. Buchanan, Y. Taur and W. Wang, IEEE, Electron Device Lett. **89**, 209 (1997).

[8] V. Ioannou-Sougleridis, G. Vellianitis, and A. Dimoulas, J. Appl. Phys. **93**, 3982 (2003).

[9] J. Robertson, J. Vac.Sci. Tech. B **18**, 1785 (2000).

[10] P.W. Peacock and J. Robertson, Appl. Phys. Lett. **83**, 2025 (2003).

[11] S. Stemmer, J.-P. Maria and A.I. Kingon, Appl. Phys. Lett. **79**, 102 (2001).

[12] J.J. Chambers and G.N. Parsons, Appl. Phys. Lett. **77**, 2385 (2000).

[13] A. Stesmans and V.V. Afanas'ev, J. Appl. Phys. **97**, 033510 (2005).

[14] J. Robertson and B. Falabretti, J. Appl. Phys. **100**, 014111 (2006).

[15] E. Atanassova, A. Paskaleva, N. Novkovski, M. Georgieva, J. Appl. Phys. **97**, 094104 (2005).

[16] A. Fissel, H.J. Osten, and E. Bugiel, J. Vac. Sci. Technol. B **21**, 1765 (2003).

[17] E.P. Gusev, E. Cartier, D.A. Buchanan, M. Gribelyuk and M. Copel, Microelectron. Eng. **59**, 341 (2001).

[18] E.P. Gusev, M. Copel, E. Cartier, I.J.R. Baumvol, C. Krug, and M.A. Gribelyuk, Appl. Phys. Lett. **76**,176 (2000).

[19] S.A. Campbell, D.C. Gilmer, X. Wang, M.T. Hsich, H.S. Kim, W.L. Gladfelter, and J.H. Yan, IEEE trans. Electron Devices **44**, 104 (1997).

[20] D.C. Gilmer, D.G. Colombo, C.J. Taylor, J. Roberts, G. Haustad, S.A. Campbell, H.-S. Kim, G.D. Wilk, M.A. Gribelyuk, and W.L. Gladfelter, Chem. Vap. Deposition **4**, 9 (1998).

[21] R.B. van Dover, Appl. Phys. Lett. **74**, 3041 (1999).

[22] A. Kumar, D. Rajdev, and D.L. Douglass, J. Am. Chem. Soc. **55**, 439 (1972).

[23] M. Copel, M. Gribelyuk, and E. Gusev, Appl. Phys. Lett. **76**, 436 (2000).

[24] H. Zhang, R. Solanki, B. Roberds, G. Bai, and I. Banerjee, J. Appl. Phys. **87**, 1921 (2000).

[25] F. Zhu, S.J. Rhee, C.Y. Kang, C.H. Choi, M.S. Akbar, S.A. Krishnan, M. Zhang, H.-S Kim, T. Lee, I. Ok, and J. C. Lee, IEEE Electron Devices Lett. **26**, 876 (2005)

[26] J. Kim, S. Kim, H. Kang, J. Choi, H. Jeon, M. Cho, K. Chung, S. Back, K. Yoo, C. Bae, J. Appl. Phys. **98**, 094504 (2005).

[27] M. Caymax, S. Van Elshocht, M. Houssa, A. Delabie, T. Conard, M. Meuris, M.M. Heyns, A. Dimoulas, S. Spiga, M. Fanciulli, J.W. Seo and L.V. Goncharova, Materials Sci. & Eng. B **135**, 256 (2006).

[28] M.A. Sahiner, J. C. Woicik, P. Gao, P. Mckeown, M.C. Croft, M. Gartman, and B. Benapfla, Thin Solid Film **515**, 6548 (2007).

[29] A. de Siervo, C.R. Flüchter, D.Weier, M. Schürmann, S. Dreiner, C. Westphal, M. F. Carazzolle, A. Pancotti, R. Landers, G.G. Kleiman, Phys. Rev. B **74**, 075319 (2006).

[30] A.Callegari, E. Cartier, M. Gribelyuk, H. F. Okorn-Schmidt, T. Zabel, J. Appl. Phys. **90**, 6466 (2001).

[31] G. D. Wilk, R.M. Wallace, J.M. Anthony, J. Appl. Phys. **89**, 5243 (2001).

[32] L.C. Feldman and J.W. Mayer, Fundamentals of Surface and Thin Film Analysis,

North-Holland, Amsterdam (1986).

[33] E. Bøgh, Phys. Rev. Lett, **19**, 61 (1967).

[34] K. Kimura, K. Ohshima, and M. Mannami, Appl. Phys. Lett., **64,** 2232 (1994).

Chapter 2

Experiments

Abstract

In this chapter, the principles of RBS are briefly explained. The experimental apparatus used in the experiments, e.g. the high-resolution RBS system, TOF-RBS system and the thermal treatment system, are described together with the preparation method of the $HfO_2/SiO_2/Si$ stack structures.

2.1 Fundamentals of RBS

In Rutherford Backscattering Spectroscopy (RBS) the primary ion energy ranges form about 100 keV (for H^+) to several MeV (for He^+ and heavier ions) [1]. The ion-atom interaction can be described using the Coulomb potential from which the Rutherford scattering cross-section is derived, which allows absolute quantification of the results. The physical basis of RBS can be described by four concepts [2].

Kinematic factor

The interaction between the projectile ion and the target atom can be properly described by a simple elastic collision of two isolated particles when the following two conditions are fulfilled.

1. The projectile energy E_0 must be much larger than the binding energy of the atom in the target. The typical binding energy is of the order of eV.

2. Nuclear reactions and resonances must be absent. With H^+ beam, nuclear effects can appear even below 1 MeV; with He^+, they begin to appear at relatively higher energies.

Using the above assumptions, we consider the collision between two particles. The projectile (mass M_1) has an incident energy E_0 and the target (mass M_2) is initially at rest, as shown schematically in Fig. 2-1.

After the elastic collision, a part of projectile energy transfers to the target nucleus. This process leads to the concept of the kinematic factor and the capability of mass perception.

The kinematics of the simple elastic collision can be fully solved by applying the principles of conservation of energy and momentum. The ratio K of the scattering energy to the incident energy can be given by

$$K = \frac{E_1}{E_0} = \left[\frac{\sqrt{M_2^2 - M_1^2 \sin^2\theta} + M_1 \cos\theta}{M_1 + M_2} \right]^2 , \qquad (2\text{-}1)$$

which is called *kinematic factor*. The scattering angle, θ, is defined as the angle between the projectile incident direction and the scattered direction as shown in Fig. 2-1. Using this formula, M_2 is able to be determined by the knowledge of the incident

particle mass M_1, the initial energy E_0, the scattering angle θ and the scattering energy E_1.

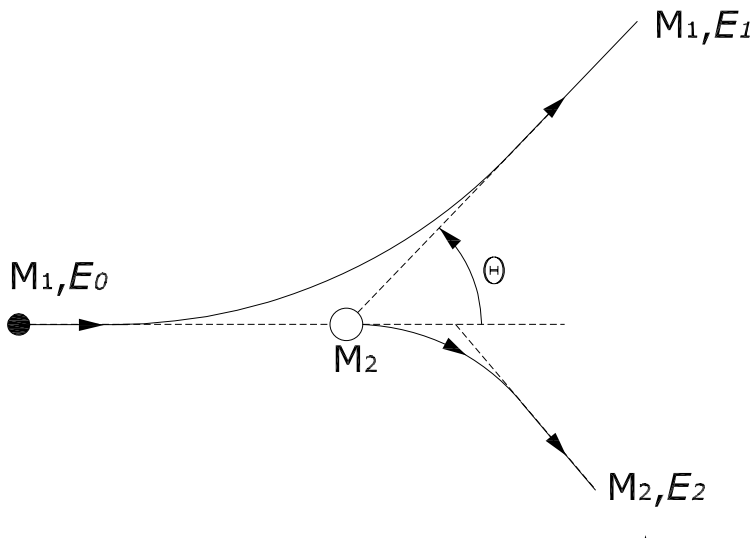

Fig. 2-1 Schematic drawing of an elastic two-body collision.

The small mass difference, ΔM_2, produces a small change ΔE_1 in the measured energy E_1 of the projectile after the collision. ΔE_1 and ΔM_2 are related to each other by:

$$\Delta E_1 \approx E_0 (dK / dM_2) \cdot \Delta M_2 . \tag{2-2}$$

Therefore, the mass resolution can be estimated from the overall energy resolution δE of the RBS as:

$$\delta M_2 = \frac{\delta E}{E_0} \left(\frac{dK}{dM_2} \right)^{-1} . \tag{2-3}$$

If the mass difference of two elements in the target falls below this limit, the distinction between two elements is lost.

Scattering Cross Section

Scattering cross section, σ, is the likelihood of occurrence of such a two-body collision. This leads to the capability of quantitative analysis of atomic composition. Using the differential scattering cross section dσ/dΩ, we can estimate how frequently such a collision actually occurs and ultimately the scattering yield at a certain angel θ.

In most cases, the force between the projectile ion and the target atom is very well described by the Coulomb repulsion of the two nuclei as long as the distance of closest

approach is large compared with nuclear dimensions, but small compared with the Bohr radius $a_B = \hbar/m_e \cdot e = 0.53\text{Å}$. When these assumptions are made, the differential scattering cross section is given by the Rutherford formula [4],

$$[d\sigma / d\Omega]_c = \left(\frac{Z_1 Z_2 e^2}{4E_0} \right)^2 \times \frac{4\left[\sqrt{(M_2^2 - M_1^2 \sin^2\theta)} + M_2 \cos\theta\right]^2}{M_2 \sin^4\theta \sqrt{M_2^2 - M_1^2 \sin^2\theta}}, \tag{2-4}$$

where Z_1 and Z_2 represent the nuclear charge of the incident particle and target atom, respectively. For a target of a thin film with a thickness of D, the scattering yield, $Y(\theta)$, detected by a finite acceptance solid angle $\Delta\Omega$ at a particular scattering angle θ can be written as:

$$Y(\theta) = N \cdot D \times \frac{d\sigma}{d\Omega} \times \frac{\Delta\Omega \cdot Q}{\cos\alpha}, \tag{2-5}$$

where Q denotes the number of incident ions impinging into the target, N stands for the atomic density of the target and α is the incident angle which is schematically shown in Fig. 2-2.

Stopping Power

An energetic particle that impinges upon a target will penetrate into it. The particle slows down and its kinetic energy decreases as it pushes its way through the target. There are two mechanisms responsible for the energy loss of the projectile: nuclear stopping which originates from a multitude of small-angle collisions of the projectile with the atomic nuclei of the target, and the electronic stopping comes from the frictional resistance that the projectile encounters on its pass through the electron clouds surrounding each target atom.

The energy loss per unit length dE/dx (usually given in eV/Å) is commonly called stopping power. The stopping cross-section S [eV/(atoms/cm^2)] is related to the stopping power and the atomic density N and is therefore more specific for a certain atomic species:

$$S = \frac{1}{N}\frac{dE}{dx}. \tag{2-6}$$

The accurate numerical predictions of stopping cross-section from theory are difficult, because of the large number of possible interactions that can conceivably take place. The most trustworthy values of S are therefore estimated by the semi-empirical formula derived from compiled experimental data. Extensive tables of stopping power data

have been collected by Ziegler *et al* [5].

The energy, E_{out}, of the ion emerging from the target surface after scattering at a depth D can be given by:

$$E_{out} = K\left[E_0 - \frac{D}{|\cos\alpha|}\cdot\left(\frac{dE}{dx}\right)_{in}\right] - \frac{D}{|\cos\beta|}\left(\frac{dE}{dx}\right)_{out}, \tag{2-7}$$

where α and β are incident angle and reflection angle which were shown schematically in Fig. 2-2. $(dE/dx)_{in}$ and $(dE/dx)_{out}$ refer to the inward path and outward path stopping power, respectively. This equation indicates that the depth D where the scattering occurred can be deduced from the observed ion energy.

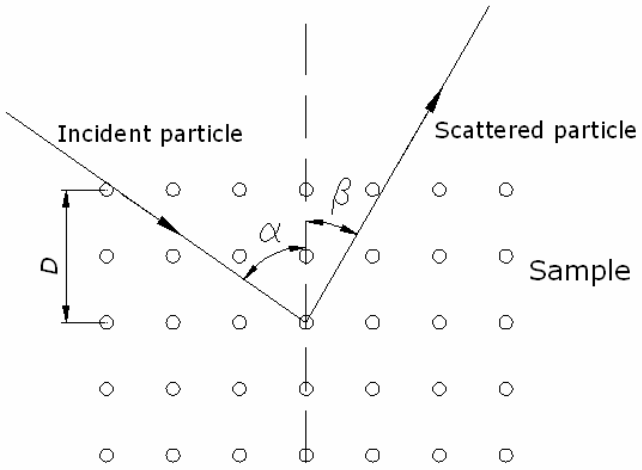

Fig. 2-2 Schematic drawing of the scattering geometry.

Using so-called energy loss factor $[S]$

$$[S] = \left[K\cdot\frac{(dE/dx)_{in}}{|\cos\alpha|} + \frac{(dE/dx)_{out}}{|\cos\beta|}\right], \tag{2-8}$$

the depth D can be given by

$$D = (E_{out} - E_1)/[S]. \tag{2-9}$$

The depth resolution is therefore given by:

$$\delta D = \delta E/[S], \tag{2-10}$$

where δE is the effective energy resolution, which is normally composed of three contributions: the energy spread of the incident beam δE_{in}, the detector resolution δE_d,

and the energy loss straggling δE_S which will be discussed in the next section. Assuming these contributions are independent, the overall resolution is given by

$$(\delta E)^2 = (\delta E_{in})^2 + (\delta E_d)^2 + (\delta E_s)^2 . \quad (2\text{-}11)$$

Energy Loss Straggling

An energetic particle that moves through a medium loses energy via many individual elastic and inelastic collisions. Such a quantized process is subject to statistical fluctuations and is accompanied by energy spreading. As a result, identical energetic particles, which all have the same initial energy, do not have exactly the same energy after pass through an identical thickness D of a homogeneous medium. The energy loss ΔE is subject to fluctuations. For long path length, the energy distribution approaches a Gaussian distribution. This phenomenon, schematically shown in Fig. 2-3, is called energy-loss straggling. This process leads to a limitation in the ultimate mass and depth resolution for RBS.

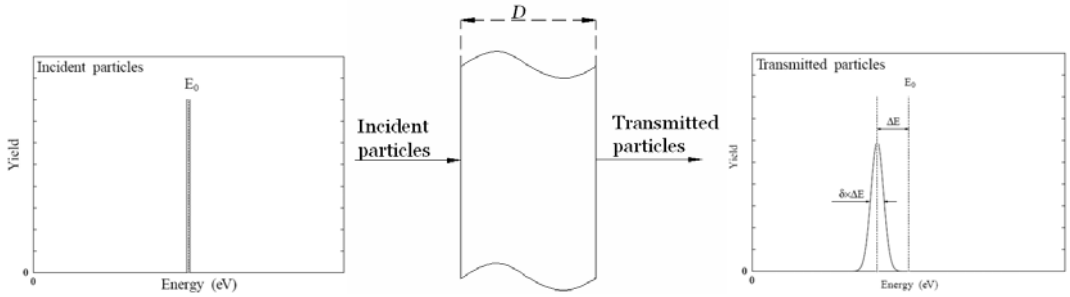

Fig. 2-3 Schematic drawing of energy straggling.

The standard deviation Ω of the energy distribution of ions passing through a medium of thickness D was given by Bohr [6],

$$\Omega_B^2 = 4\pi Z_1^2 Z_2 e^4 ND . \quad (2\text{-}12)$$

This formula stands for the high-energy limit and it has been extended to lower energies by many authors. A useful formula was given by Lindhard and Scharff [7]

$$\frac{\Omega^2}{\Omega_B^2} = L(\chi) = \begin{cases} 0.68\chi^{1/2} - 0.08\chi^{3/2} & \chi \le 3 \\ 1 & \chi \ge 3 \end{cases} , \quad (2\text{-}13)$$

where $\chi = (V/v_B)^2/Z_2$, V is the ion velocity, and v_B the Bohr velocity. The contribution of the energy-loss straggling to the energy resolution is given by

$$(\delta E_S)^2 = 8\ln 2(K(\theta)^2 \Omega_{in}^2 + \Omega_{out}^2) , \quad (2\text{-}14)$$

where 8ln2 is a conversion factor from the standard deviation to the full width at half maximum, and Ω_{in} and Ω_{out} are the straggling in inward and outward paths.

2.2 Setup of HRBS system with a magnetic spectrometer

In the present investigation a HRBS system, including a 400 kV Cockcroft-type accelerator, a magnetic spectrometer, a one-dimensional micro-channel-plate position sensitive detector (1D-PSD) and electronic modules for the detector, were used. The setup without the electronics is shown schematically in Fig. 2-4. The red line shows the trajectory of the ion beam during the measurement.

An ion source of PIG type and the acceleration tube are enclosed in an isolation tank of diameter 0.6 m and height 1.5 m which is filled with SF_6 gas. The He^+ ion beam generated by the accelerator, with energy of 400 keV, is mass analyzed and is collimated by two sets of four-jaw slits separated by 1.2 m each other in the beam line. The typical beam current is about 70 nA with a square shape of about 2×2 mm^2 in size. An ultra high vacuum (UHV) scattering chamber (base pressure 4×10^{-10} Torr) is connected to the beam line via a differential pumping system [8]. Specimens are mounted on a five-axis high precision goniometer in the UHV chamber. Ions scatted from the specimen are energy analyzed by the magnetic spectrometer and detected by the 1D-PSD placed on the focal plane of the spectrometer.

The spectrometer is basically a standard 90° sector type with 26.6° inclined boundaries for two dimensional focusing. The bending radius of the spectrometer is 200 mm and the maximum bending power (mE/q^2) is 1.75 MeV·amu/e^2. The acceptance angle of the spectrometer is variable up to 4×10^{-4} sr. After disconnection of the spectrometer from the UHV chamber the spectrometer can be easily rotated around the chamber to change the scattering angle. In this investigation, the scattering angle was set to be 50° and 75°. The standard spectrometer with 26.6° inclined boundaries has a focal plane being inclined at about 60° with respect to the optical axis, leading to low detection efficiency of 1D-PSD. In order to improve the efficiency the exit boundary is modified from a straight line so that the focal plane is perpendicular to the optical axis. Combining with a 1D-PSD of length 100 mm, the energy range of 25% of the central energy can be measured without sweeping the magnetic field. The energy resolution of the spectrometer is designed to be less than 0.1% (0.4 keV at 400 keV) at an acceptance angle of 0.4 msr. The spectrometer has an electrostatic quadrupole lens

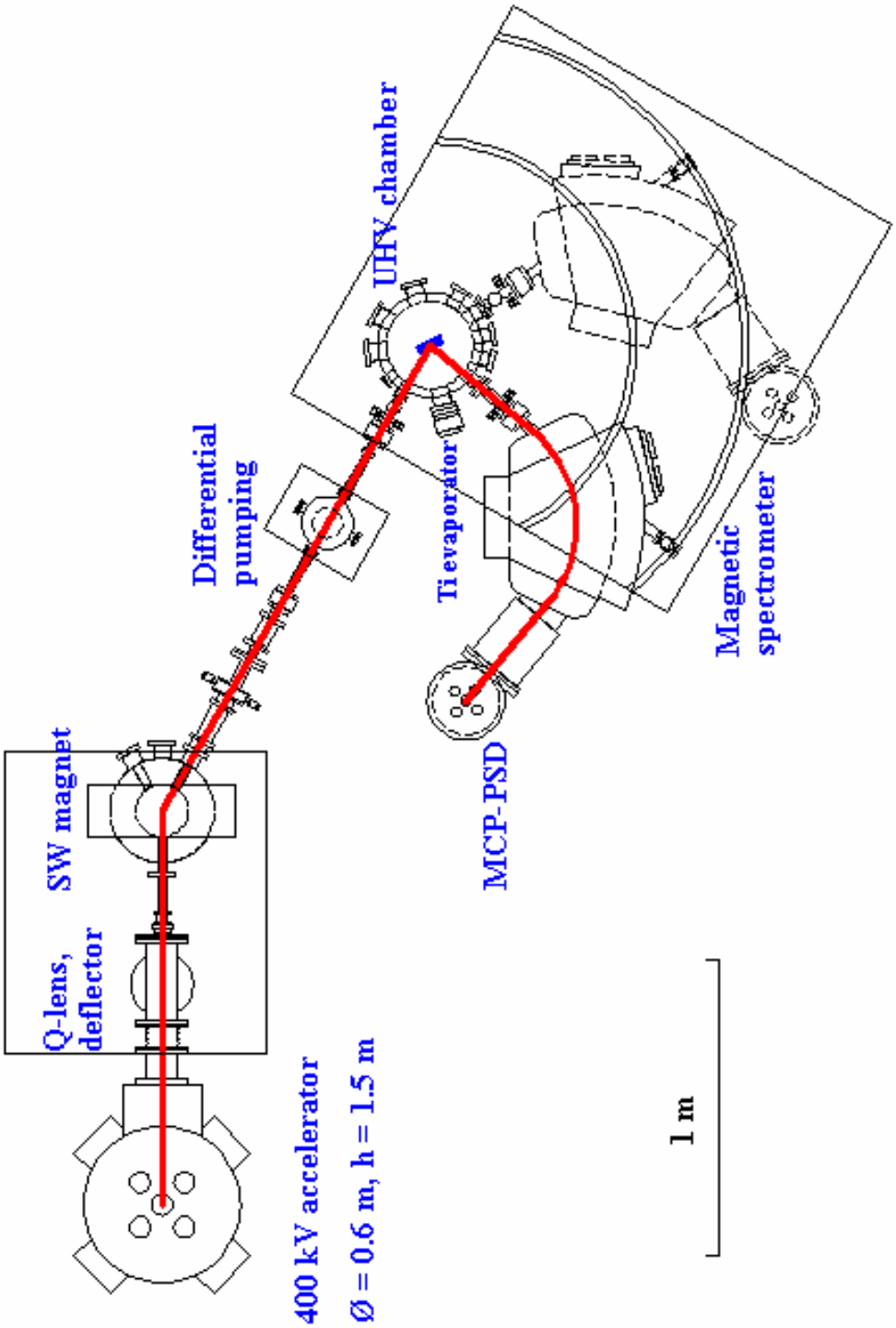

Fig. 2-4 Schematic drawing of the Kyoto Univ. HRBS system

just before the entrance of the sector magnet providing the correction for kinematic broadening to get high depth resolution for light element analysis [8].

The signal processing system employed for the 1D-PSD is shown in Fig. 2-5.

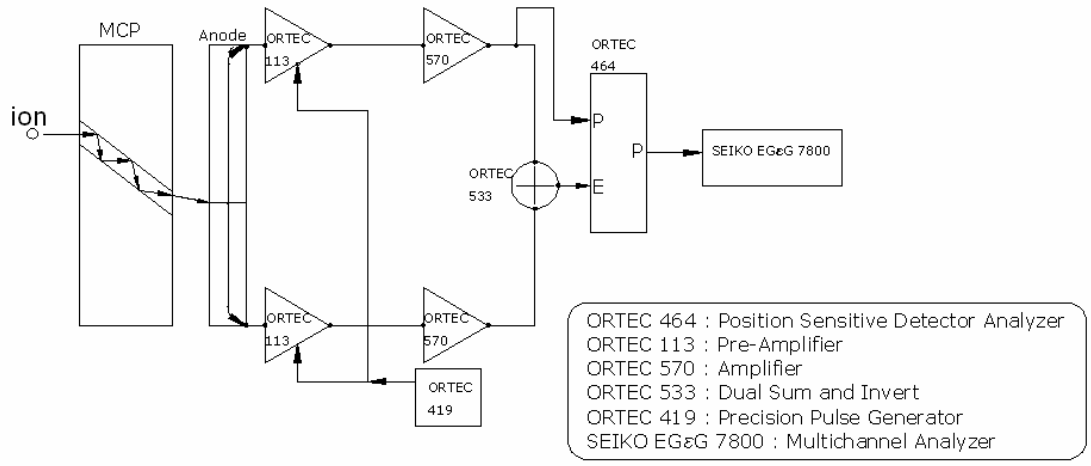

Fig. 2-5 The signal processing system employed for the 1D-PSD in the HRBS system.

2.3 Thermal treatment systems

In this investigation, an infrared furnace was mainly used for annealing the samples. In addition, some of the samples were annealed in situ in the UHV scattering chamber either by a tungsten heater mounted on the goniometer or by the DC resistive heating.

The infrared furnace (MILA 3000-P-N) could heat the sample up to 1200 °C (in vacuum) with a maximum heating speed of 50 °C/sec (in vacuum). The whole system is cooled by flowing water for precise control of temperature. The temperature was measured by the thermocouple and the error was less than 4 °C. The heating chamber could be evacuated by a turbo molecular pump (TMP) and the base pressure was ~1.0×10^{-5} Torr. The heating chamber was connected to two oxygen providing systems for $^{18}O_2$ and $^{16}O_2$. Thus the heating atmosphere could be the air, the vacuum or other specific gas, i.e. $^{18}O_2$ or $^{16}O_2$. The schematic drawing of the infrared furnace is shown in Fig. 2-6.

The tungsten heater and the resistive heating setup are both used for annealing under the UHV condition, and are both mounted on the goniometer installed in the UHV scattering chamber of the HRBS system. The temperature of the sample during the annealing was measured by an infrared thermometer. The error of the temperature measurement was ~10 °C.

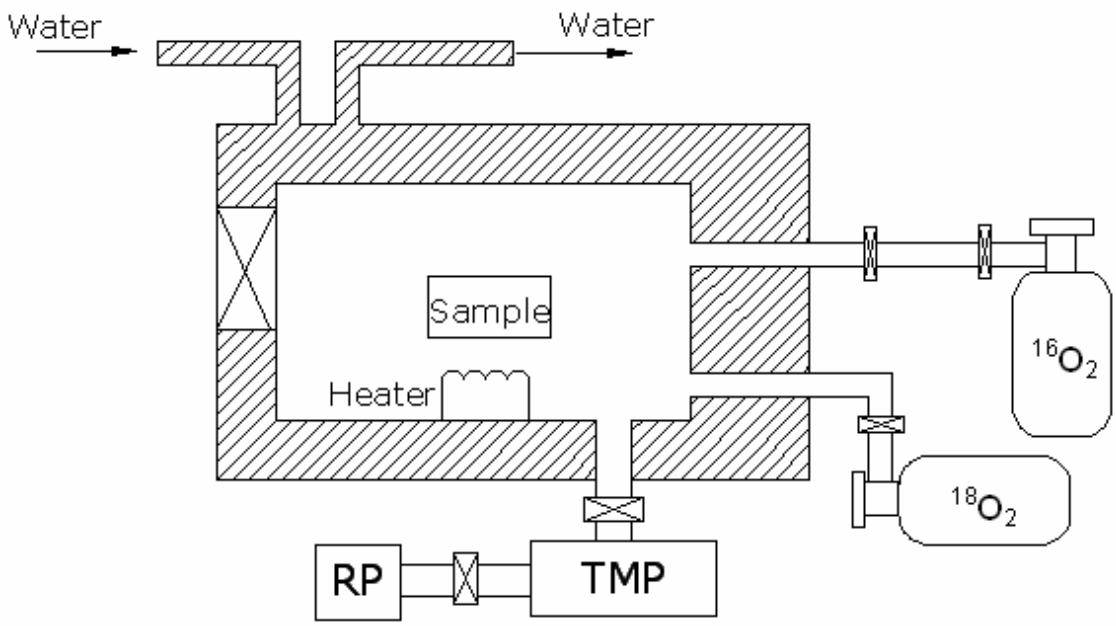

Fig. 2-6 Schematic drawing of the infrared furnace.

2.4 Preparation of $HfO_2/SiO_2/Si$ stacks

A HfO_2 film of 4 nm thickness was grown by atomic layer deposition (ALD) using tetrakis (ethylmethylamino) hafnium ($Hf[N(CH_3)(C_2H_5)]_4$) with O_3 as an oxidant after preparing a SiO_2 layer of 0.7 nm thickness on Si(001). In order to prepare a high quality HfO_2 film, the samples were annealed in O_3 at 275 ˚C for 10 min (sample-1) or in O_2 at 1000 ˚C for 10 sec (sample-2) after deposition [9]. These samples thus prepared are called as-grown sample in this thesis.

The as-grown samples were annealed in an infrared furnace (MLLA 3000-P-N) at 500-900 ˚C in oxygen atmosphere for 30 sec to 20 min. For crystallization of HfO_2, some samples were annealed in the UHV chamber (base pressure ~ 4×10^{-10} Torr) at 800 ˚C for 10 min as a pre-process treatment.

Ti was deposited on the $HfO_2/SiO_2/Si$ stack by resistive heating of Ti wire (purity 99.9%) in situ in the UHV scattering chamber. Thin Ti layer was grown and subsequently annealed at ~330 ˚C for 30 min in the UHV chamber.

2.5 Setup of RBS with Time-of-Flight (TOF) system

The precise characterization of the structure and the composition in the high-*k* stack structures especially in the near-surface region is strongly required in microelectronics

industry. The Rutherford backscattering spectroscopy (RBS) is one of the most promising surface analysis methods for such requirement [1]. For the analysis of the crystallographic information, channeling and/or blocking techniques can be used. The HRBS system described in Section 2.2, however, is not a suitable system for the blocking measurement, because it cannot measure the angular distribution of scattered ions.

A new HRBS system, which is capable to measure angular and energy distributions simultaneously, was developed for the analysis of the crystallographic information of the surface area of the sample. The system was based on the time of flight (TOF) technique, and consists of an accelerator, a beam chopping system, a scattering chamber, and a two dimensional delay-line detector with a diameter of 120 mm (RoentDek, DLD120). This new HRBS system, which will be referred to as TOF-RBS, can provide both the energy spectrum and the angular distribution of the scattered ions simultaneously. The schematic drawing of TOF-RBS system is shown in Fig. 2-7, where the red line represents the trajectory of the ion. The 100 keV He^+ ion beam was generated by the accelerator and collimated as was in the HRBS system, which was described in Section 2.1.2.

The beam chopping system is mounted along the beam tracing line between the accelerator and the sample, which produces a pulsed ion beam. The beam chopping system is constituted by:

- Two parallel electric field plates horizontally separated by 4.25 mm to each other and aligned with the beam line.
- Entrance slit placed just before the parallel electric field plates with a hole of 1 mm in horizontal direction.
- Exit slit with a hole of 0.6 mm in horizontal direction placed 1570 mm behind the electric field plates.
- High-voltage pulse generator (Kentech Instruments Ltd.).

The pulse generator could provide rectangular pulses up to ± 450 V (see Fig. 2-8) with repetition rates up to 500 kHz. The rise and fall times were less than a few ns. The pulse generator also provides *timing signals* at the leading and trailing edges of the rectangular pulse, which was used as the *start signal* in the TOF measurement.

A typical ion measurement is schematically depicted in Fig. 2-8. In the beam chopping, the rectangular pulses (-375 V to +375 V) with repetition rates up to 500 kHz

were sent to the right electric field plate while the left plate was grounded. The ion beam can pass through the exit slit only at the rising and falling edges of the pulses, i.e. rectangular pulse, which was used as the *start signal* in the TOF measurement.

A typical ion measurement is schematically depicted in Fig. 2-8. In the beam chopping, the rectangular pulses (-375 V to +375 V) with repetition rates up to 500 kHz were sent to the right electric field plate while the left plate was grounded. The ion beam can pass through the exit slit only at the rising and falling edges of the pulses, i.e. only during the ion beam is swept from right (left) to left (right) direction. This process produces pulsed beam with a repetition rate twice faster than the pulse repetition rate.

The 2D-DLD can measure the detected position with a resolution of 0.1 mm. Thus the angular distribution of the scattered ions can be obtained from the measured position distribution. The 2D-DLD can also measure the detection time with a time resolution of 0.13 ns. Using the timing signal from the pulse generator as the reference, the flight time of the scattered ion between the target and the detector can be estimated and so the energy spectrum of the scattered ions can be derived.

The pulsed beam is incident on the target and the scattered ions are detected by the detector placed 506 mm from the target. The detector system consists of the following components:

- Micro-channel plates (MCPs) and a delay-line anode
- DLA-TR6 module (amplifiers)
- HM1-B (time-to-digital-converter, TDC)
- Data acquisition and data analyzing software CoboldPC

The MCP with two delay-line anodes constitutes two dimensional position and time sensitive multi-hit detector (shortly called as 2D-DLD in this work). It has a diameter of 120 mm, a position resolution of < 0.1 mm, a time resolution of 0.13 ns, a rate capability of 1 MHz, and a multi-hit resolution of 20 ns. Its working pressure should be $<1.5\times10^{-6}$ Torr.

The typical voltage settings for detector are the following:

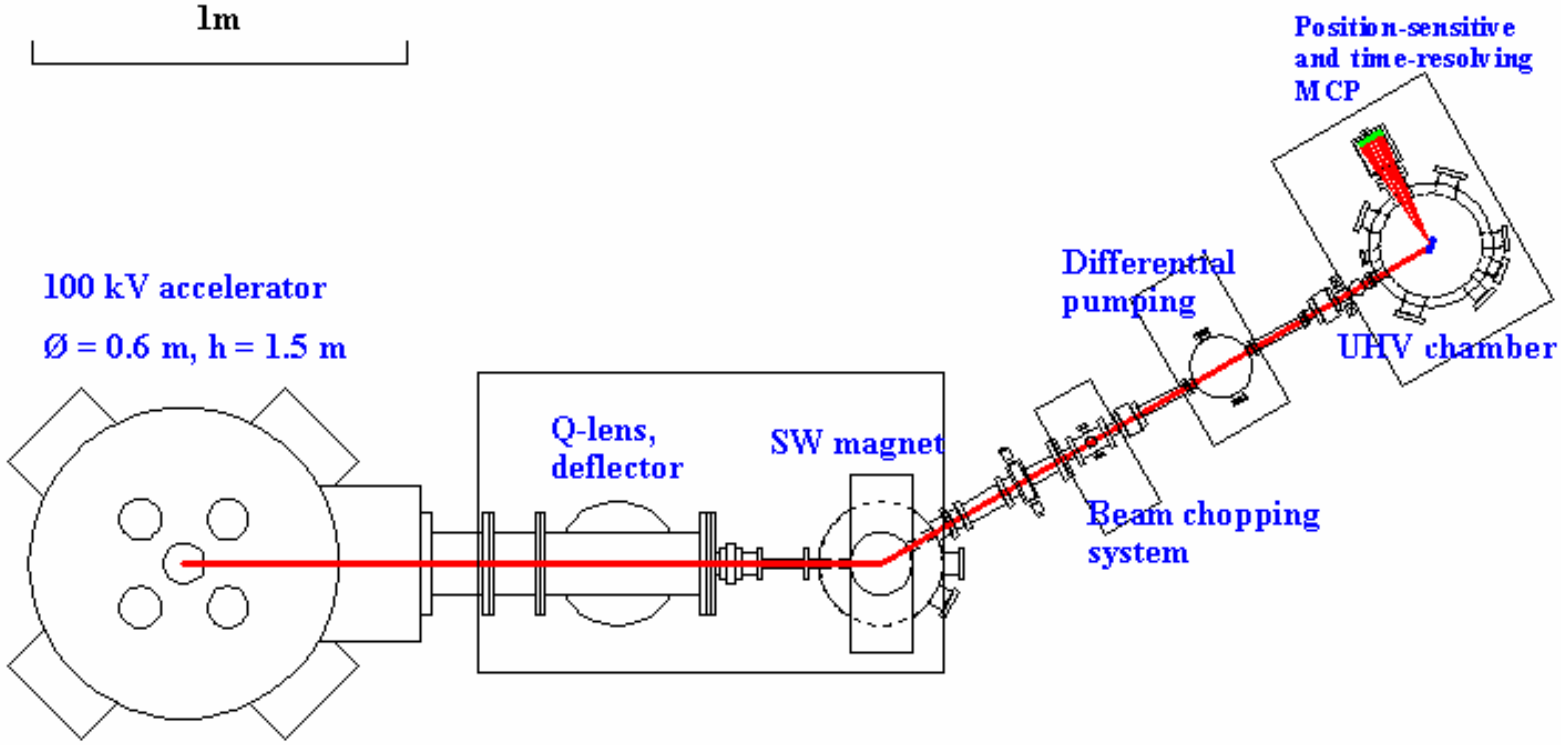

Fig. 2-7 The schematic drawing of TOF-RBS system.

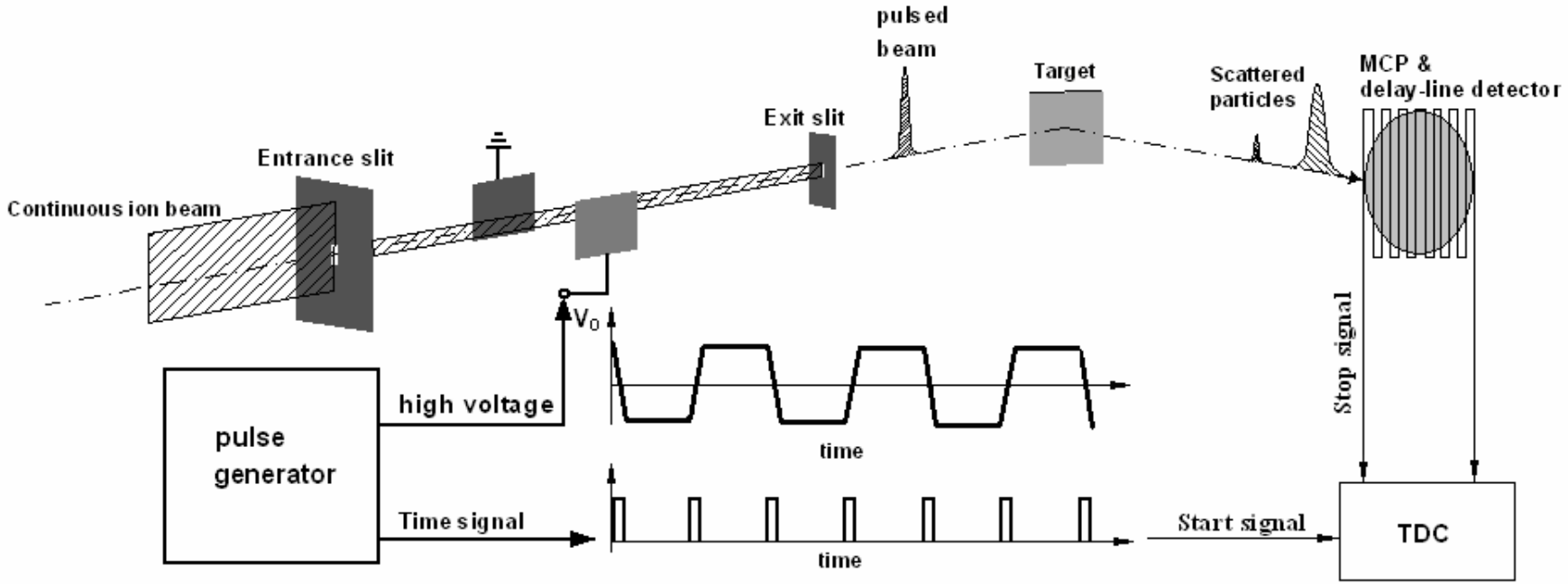

Fig. 2-8 Schematic depiction of an ion scattering measurement using TOF-RBS syetem.

MCP front	-2400 V
MCP back	0 V
Anode holder	+150 V
Reference wires	+ 480 V
Collecting (Signals) wires	+500 V

The operation principle of the delay-line anode is schematically shown in Fig. 2-9. When the 2D-PSD detected the ion, MCPs amplify the electronic signal and sends these signals to the delay-line anode. There are two sets of delay-line anode for the two dimensional measurement. The electronic signal separate into two signals in the delay-line anode and they arrive the anode ends at different times, which are denoted by x1(y1) and x2(y2).

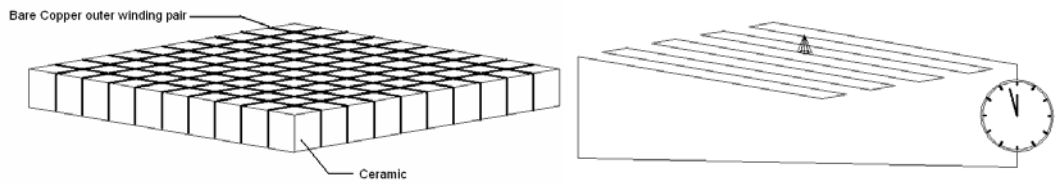

Fig. 2-9 Operation principle of the delay-line anode.

The signal processing system employed for the 2D-DLD in the TOF-RBS system is shown in Fig. 2-10. The dashed line encircles the modules that belong to DLA-TR6.

The DLA-TR6 module is a 6-channel differential amplifier. The output timing signal has a precision below 50 ps. It is designed to read-out the delay-line detectors and amplify the timing signals. The amplified timing signals, x1(y1) and x2(y2), were sent to HM1-B as the *stop signal*. The HM1-B module is a time-to-digital-converter (TDC) used for time interval measurement. HM1-B has a common-start input and 4 channels of stop inputs. The time resolution of the HM1-B is 150 ps or better.

After the start signal is received, HM1-B waits a certain time period (event waiting time) for stop signals. The particles arriving within this event waiting time will be treated as a successful event. The time intervals between the *start* and *stop signals* for the successful event are converted into digital signals and stored in the internal memory of HM1-B. The stored events are sent to PC when PC requires.

The digital signals sent to the PC are processed and displayed by the soft ware CoboldPC. Time difference between x1(y1) and x2(y2) corresponds to the position of

the ion. Half of the sum of x1(y1) and x2(y2) represents to the time that the ion collided on the 2D-DLD.

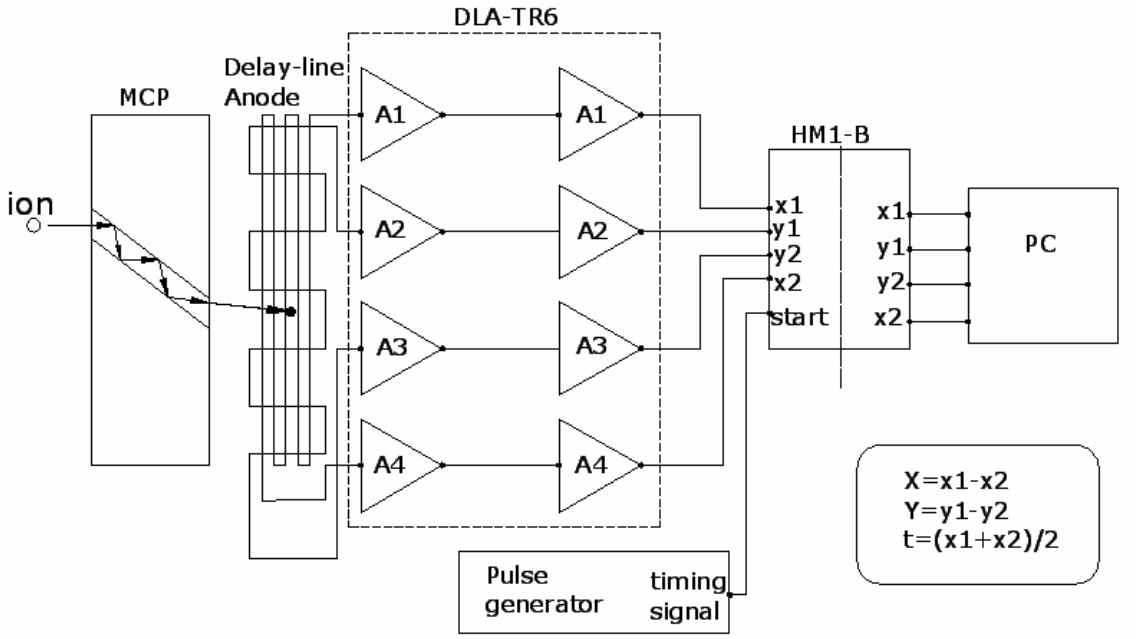

Fig. 2-10 The signal processing system employed for the 2D-PSD in the TOF-RBS system.

References

[1] John. C. Vickerman, Surface Analysis – The Principal Techniques, John Wiley & Sons, Chichester (1997).

[2] W.-K. Chu, J. W. Mayer and M.-A. Nicolet, Backscattering Spectrometry, Academic press, New York (1978).

[3] E Rutherford, Phil. Mag. **21**, 669 (1911).

[4] C.G. Darwin, Phil. Mag. **28**, 499 (1914).

[5] J.F. Zirgler, Helium Stopping Powers and Ranges in All Elemental Matter, Pergamon Press, New York (1977).

[6] N. Bohr, The Penetration of Atomic Particles through Matter, Kgl. Danske Videnskab. Matt-Fys. Medd. **18**, 8 (1948).

[7] J. Lindhard, M. Scharff, Energy Loss in Mater by Fast Particles of Low Charge, Kgl. Danske Videnskab. Matt-Fys. Medd. **27**, 15 (1953).

[8] K. Kimura, S. Joumori, Y. Oota, K. Nakajima, M. Suzuki, Nucl. Instrum. Methods Phys. Res. B **219-220**, 351 (2004).

[9] S. Kamiyama, T. Miura, and Y. Nara, Appl. Phys. Lett., **87**, 132904 (2005).

Chapter 3

Si emission from the SiO_2/Si interface during the growth of SiO_2 in the HfO_2/SiO_2/Si structure

Abstract

HfO_2/SiO_2/Si(001) structures were annealed in dry oxygen, and compositional depth profiles were measured by high-resolution Rutherford backscattering spectroscopy. Growth of the interfacial SiO_2 layer and simultaneous surface accumulation of Si were observed. The observed result indicates that silicon species are emitted from the SiO_2/Si interface to release the stress induced by oxidation as was predicted by recent theoretical studies.

3.1 Introduction

The down scaling of Si devices has led to the need for fine control techniques to form oxide layer as thin as 1 nm. Therefore, an understanding of Si oxidation is strongly demanded by the industry as well as in materials science [1]. This is also the case even if SiO_2 is replaced by high-*k* materials in the future Si devices. An ultrathin (sub nm) SiO_2 layer is intentionally grown on Si before the formation of the high-*k* film to get better device performance [2]. Thus, the understanding of Si oxidation is still an important issue.

The oxidation of relatively thick (> 10 nm) films is well described by the so-called Deal-Grove model [3]. The oxidation kinetics for very thin films, however, cannot be explained by the Deal-Grove model [4]. The oxidation rate for thin films is much faster than that expected from a linear relationship predicted by the Deal-Grove model. The failure of the Deal-Grove model may be related to the large volume expansion upon oxidation. During oxidation of Si, oxidant diffuses through the disordered oxide network and reacts with silicon substrate at the SiO_2/Si interface [3, 5 - 7]. The volume of the increased oxide region is about twice larger than that of the decreased Si region. The volume expansion results in high stress on the interface between Si and SiO_2 [8, 9], which should be released when the oxidation proceeds. Recent theoretical studies predicted that Si species are emitted from the SiO_2/Si interface into the SiO_2 to reduce the stress [10, 11]. Most of the emitted Si species diffuse into and through the SiO_2. Depending on the SiO_2 layer thickness, emitted Si species accumulate at the surface as a new oxide layer (in case of thin films) or they are incorporated in the SiO_2 layer through oxidation (in case of thick films) [12]. There are several experimental results consistent with this scenario [13, 14]. Nevertheless, there is no direct observation of the predicted Si emission so far.

In the present work, we use HfO_2/SiO_2/Si structures to observe the Si emission. It is known that the interfacial SiO_2 layer grows during the high-temperature thermal processing of the high-*k*/SiO_2/Si structures in oxygen ambient [15]. Here, we observe the behavior of Si atoms during the growth of the interfacial SiO_2 layer using high-resolution Rutherford backscattering spectroscopy (HRBS). A recent study on the thermal decomposition behavior of HfO_2/SiO_2/Si indicates that Si species can out-diffuse through a HfO_2 film [16]. The emitted Si species from the SiO_2/Si interface, therefore, are expected to accumulate at the surface of the HfO_2 film. Thus, the emitted Si can be separately observed from the interfacial SiO_2 layer using HRBS.

3.2 Experimental

The sample-1 described in Section 2.4 was used in this study. The as-grown sample-1 [17] was annealed in the infrared furnace (MLLA 3000) at 500 - 900°C in dry $^{16}O_2$ for 2 - 20 minutes. For comparison, the as-grown sample-1 was annealed also in the UHV chamber (base pressure 4×10^{-10} Torr) at 800°C for 2 minutes by resistive heating.

These samples were observed by HRBS using 400 keV He^+ ions as a probe. Since the details of the HRBS system [18] have been reported in Chapter 2, we only briefly describe the measurement condition. In the present measurements, the samples were aligned to a channeling configuration with the [111] axis parallel to the incident beam, reducing the substrate contribution to the signal. Energy spectra of He^+ ions scattered at 50° were measured by a 90° sector magnetic spectrometer.

3.3 Results and discussion

3.3.1 Characteristic of as-grown sample-1 by HRBS

When the incident beam is aligned to a major symmetry direction of a single crystal, i.e. low index axis or plane, so-called *channeling* occurs. Channeled particles cannot get close enough to the atomic nuclei to undergo large angle Rutherford scattering; hence, scattering from the crystal is drastically reduced by a factor of ~100 [19]. By measuring the reduction in backscattering yield for channeling, it is possible to quantitatively measure and profile the crystal perfection of a sample and to determine its crystal orientation. Channeling also improves the sensitivity to light elements in an amorphous or poly-crystal layer formed on a single crystal surface. For the depth profiling of elements in a single crystal sample (e.g. profiling of Si in the present case), however, channeling should be avoided for quantitative analysis. In order to avoid the channeling effect the sample was rotated around the normal direction of the surface during the measurement. The spectrum, thus obtained is called a *random* spectrum.

Figure 3-1 shows the observed random (a) and channeling (b) HRBS spectra. There are two peaks in the random spectrum. The large peak at ~390 keV corresponds to Hf in the HfO_2 layer. The peak seen at ~330 keV corresponds to ^{16}O in both the HfO_2 and the interfacial SiO_2 layers. Because the oxygen peak overlaps with the high intensity Si signal, precise extraction of oxygen signal is rather difficult. The [111] channeling configuration was used to reduce the signals from the silicon substrate. As the result, oxygen peak can be observed more clearly. This allows precise analysis of oxygen.

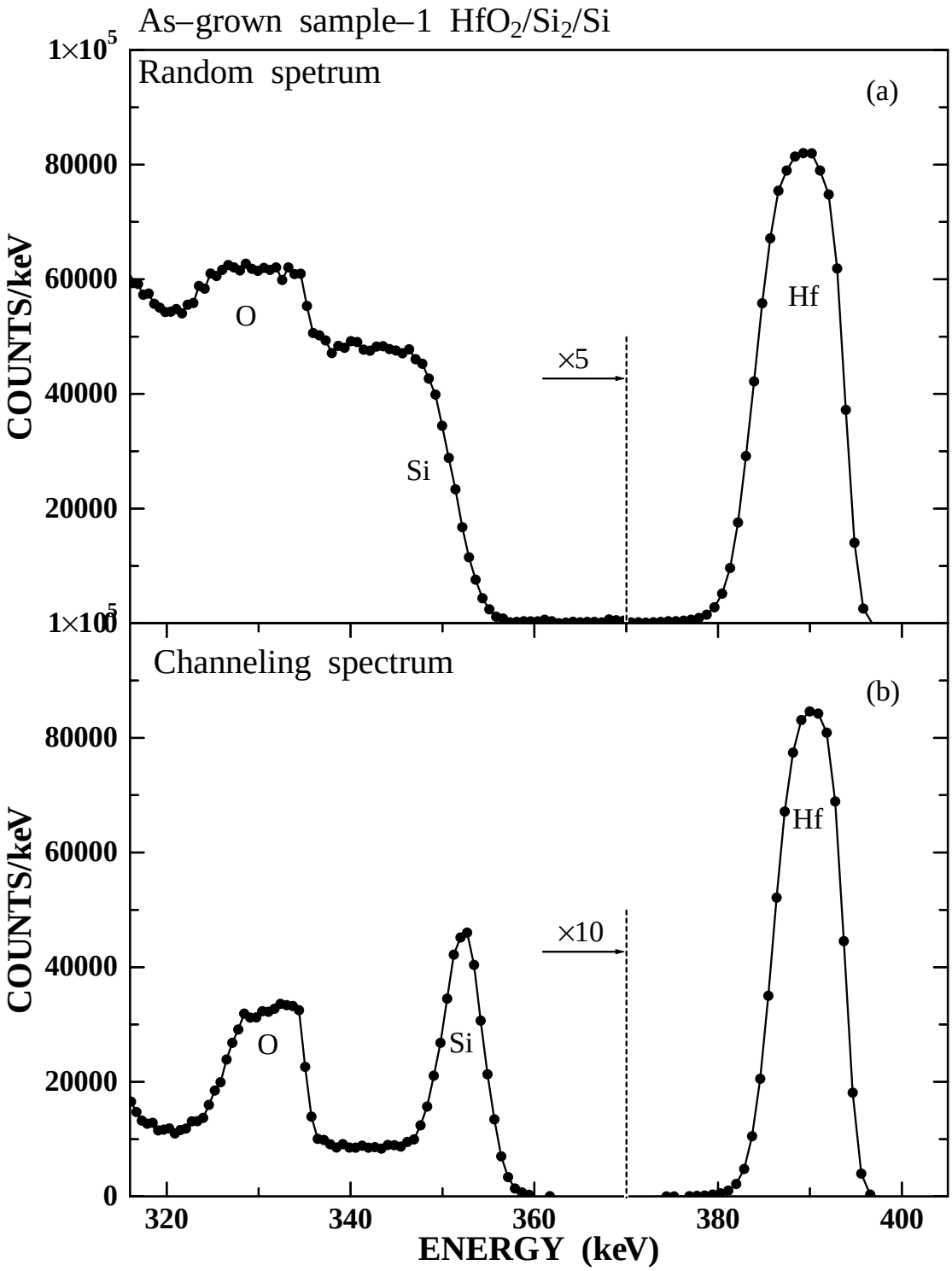

Fig. 3-1 The HRBS energy spectra observed under random conditions (a) and [111] channeling conditions (b) of the as-grown sample-1. The incident ion was 400 keV He^+ and the angle of incidence were 59.24 and 54.74° for random and channeling conditions, respectively. The scattering angle was 50°.

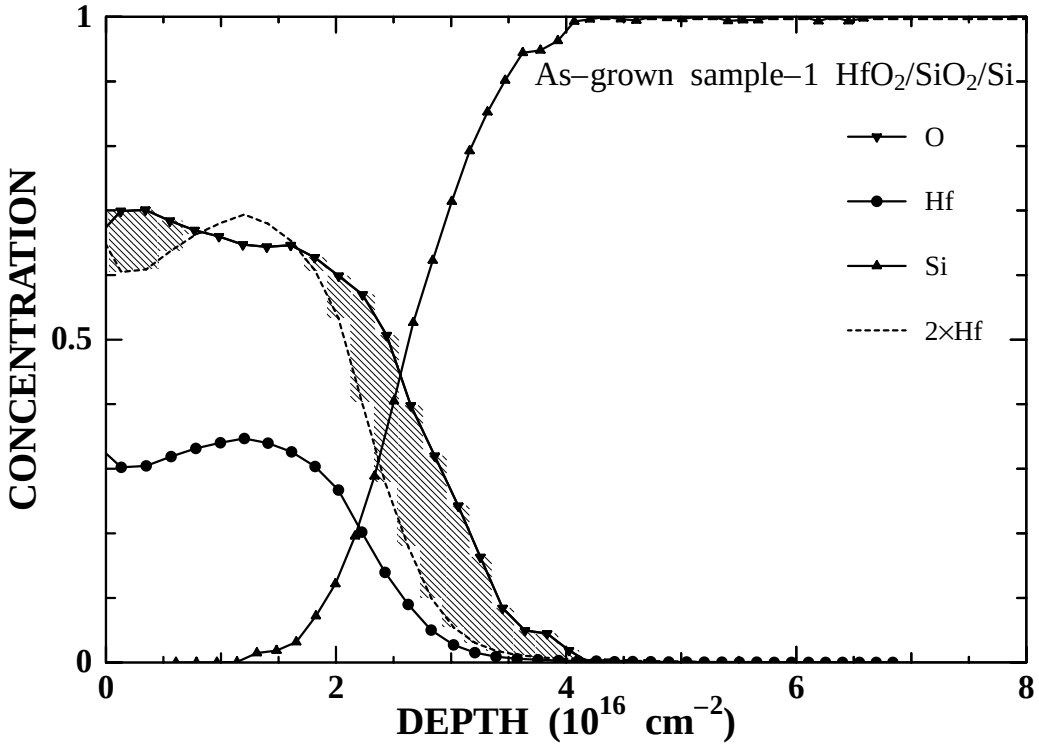

Fig. 3-2 The depth profiles of elements in the as-grown sample-1.

The silicon peak can be seen at 350 keV that corresponds to Si in the SiO_2/Si interface region. This Si interface peak consists of contribution from the interfacial SiO_2 layer and the substrate Si atoms which can be seen by the channeling ions. The latter contribution mainly comes from the topmost Si atomic layer in the substrate Si (this is essentially the same as the so-called surface peak in a usual channeling spectrum) and is almost independent of the thickness of the interfacial SiO_2 layer unless the SiO_2 layer is extremely thick. In the channeling spectrum, the oxygen peak and the hafnium peak are similar to those in the random spectrum. From these observed HRBS spectra depth profiles of the constituent elements were derived. The obtained depth profile of the as-grown sample-1 was shown in Fig. 3-2. The dashed line shows twice the Hf concentration, which roughly agrees with the oxygen concentration. This means that almost stoichiometric HfO_2 layer was grown. There are, however, excess oxygen atoms in the interface region (shaded area), which correspond to the interface SiO_2 layer. The thickness of the HfO_2 layer and SiO_2 layer are estimated to be 3 nm and 0.7 nm from the observed results, respectively.

3.3.2 Si outward emission during the interface SiO_2 growth

Figure 3-3 shows the change in the HRBS energy spectrum induced by annealing. The solid line shows the spectrum of the as-grown sample-1. The spectrum of the sample annealed at 800 °C in 0.1Torr O_2 for 2 min (short dashed line in Fig. 3-3) is quite different from that of the as-grown sample-1. Both the Si peak as well as the O peak become wider after annealing, indicating the growth of the interfacial SiO_2 layer. The increase of the interfacial SiO_2 layer is estimated to be 0.6 nm from the observed Si peak. In contrast to the Si and the O peaks, the shape of the Hf peak does not change but a small shift (~ 0.3 keV) towards lower energies is observed. A similar shift was also observed for the leading edge of the Si interface peak. These shifts suggest the formation of an overlayer on the HfO_2 surface. In addition to these changes, a new peak appears around 361 keV, which corresponds to Si at the surface. The amount of the surface Si is estimated to be 3.3×10^{14} atoms/cm^2 (corresponding to a SiO_2 layer of 0.14 nm thickness). The energy shift of the Hf peak due to the formation of a 0.14 nm SiO_2 overlayer is calculated to be 0.27 keV. This is in good agreement with the observed energy shift, suggesting that SiO_2 overlayer of 0.14 nm thickness was formed on the HfO_2 layer.

However, there could be an alternative explanation of the surface Si signal, i.e. pinholes might be formed in the HfO_2 film during oxidation [20]. In order to eliminate this

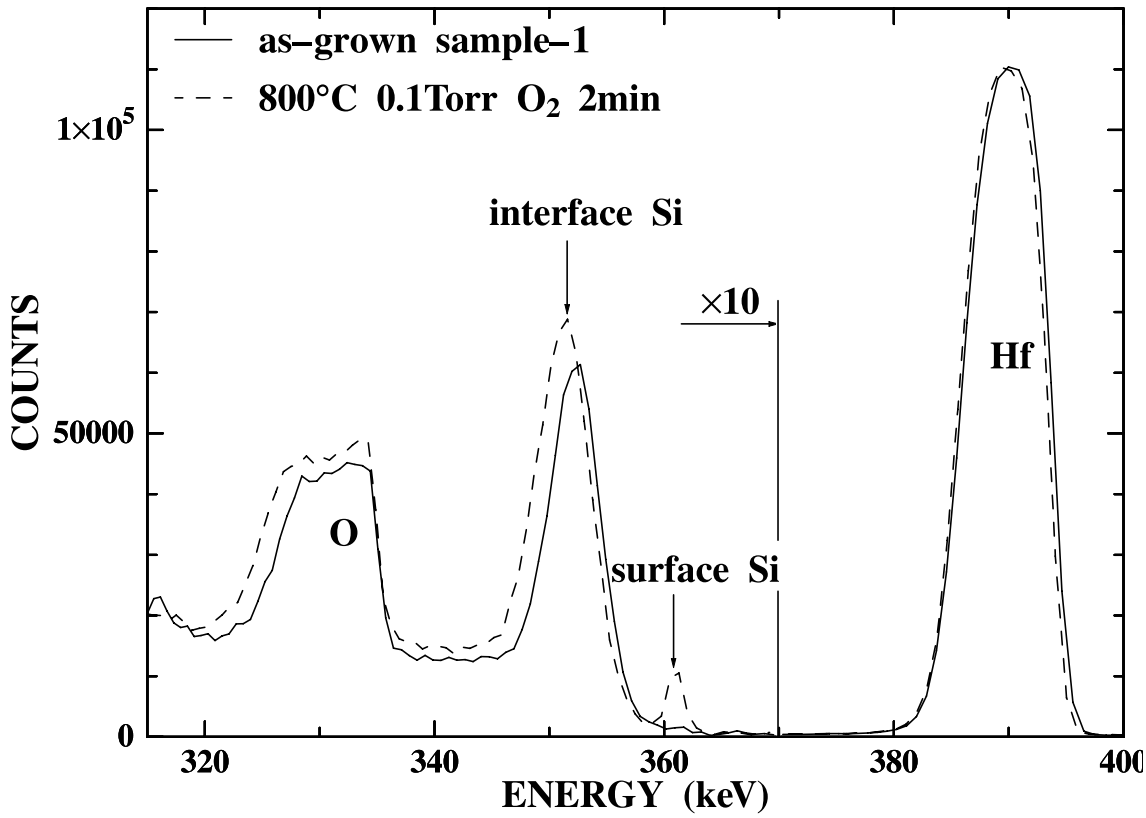

Fig. 3-3 HRBS energy spectra observed under [111] channeling conditions for the as-grown sample-1 $HfO_2/SiO_2/Si(001)$ (solid line) and the sample annealed at 800°C for 2 minutes in 0.1 Torr O_2 (dashed line). The incident ion was 400 keV He^+ and the angle of incidence and the scattering angle were 54.74° and 50°, respectively.

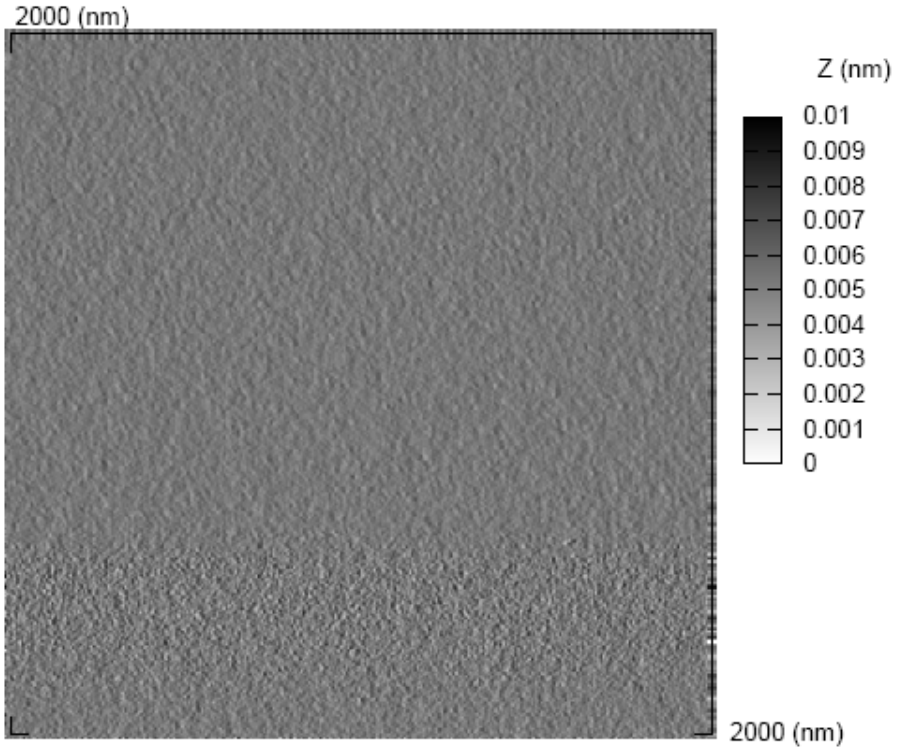

(a)

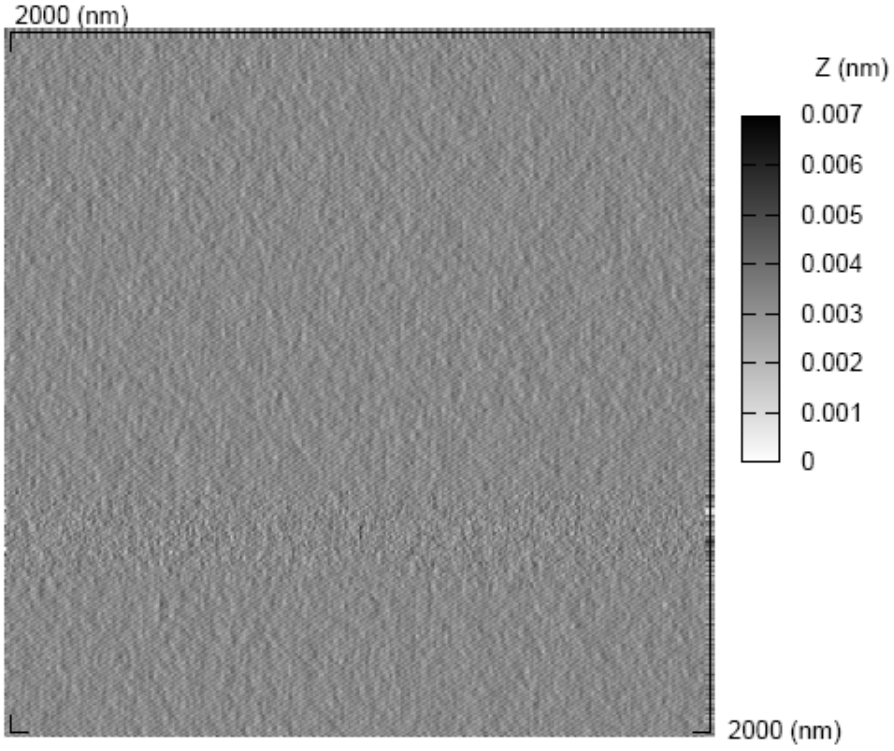

(b)

Fig 3-4 AFM pictures of as-grown sample-1 (a) and the sample annealed at 800 °C in 0.1 Torr O_2 for 2 min (b).

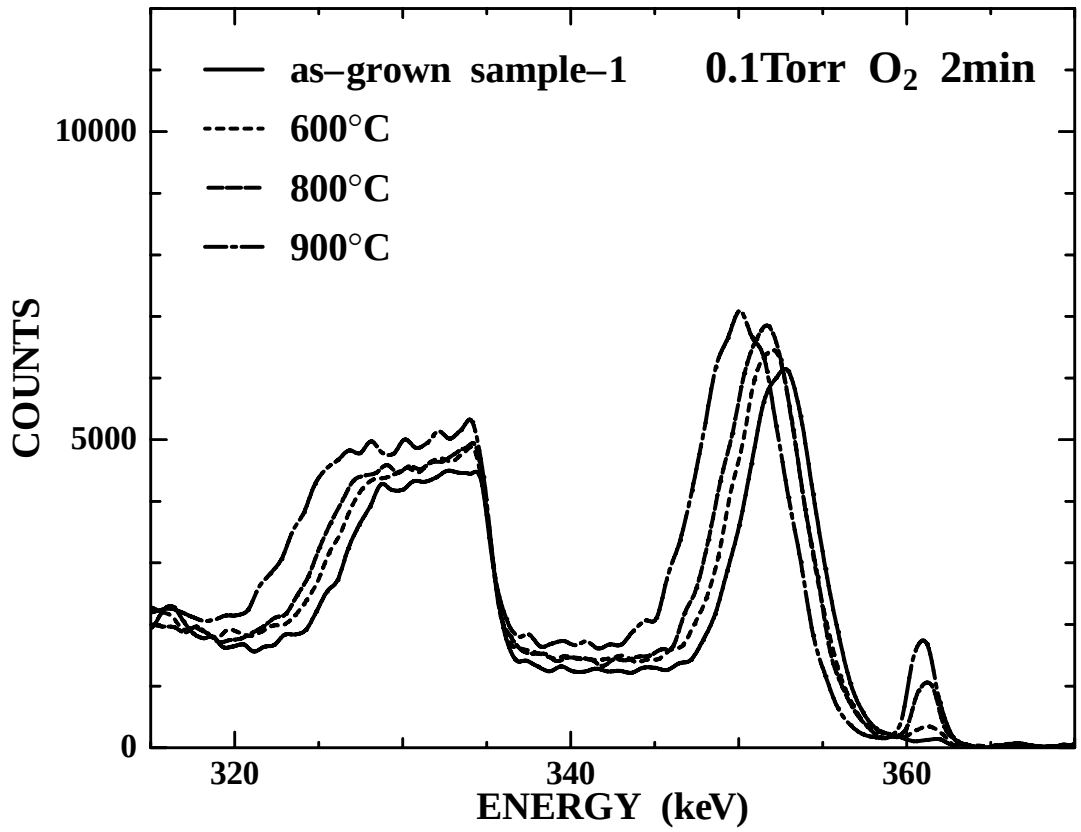

Fig. 3-5 HRBS energy spectra observed under [111] channeling conditions for as-grown sample-1 $HfO_2/SiO_2/Si(001)$ (solid line) and samples annealed at various temperatures in 0.1 Torr O_2 for 2 minutes; 600°C (short dashed line), 800°C (dashed line) and 900°C (dot-dashed line). The incident ion was 400 keV He^+ and the angle of incidence and the scattering angle were 54.74° and 50°, respectively.

possibility, the surface of the sample was examined using atomic force microscopy (AFM) and scanning electron microscopy (SEM). Figure 3-4 shows the AFM images of the as-grown sample-1 and the sample annealed in 0.1 Torr at 800 °C for 2 min. No pinhole was observed in either of the images, confirming the formation of SiO_2 overlayer on HfO_2. In addition, there was also no signature of void formation at the oxide/silicon interface in the observed AFM and SEM images.

The hafnium peak kept the same shape after annealing indicating that the HfO_2 layer has very good thermal stability in contact with silicon during thermal process at the temperature of 800 °C, even in oxygen containing atmosphere.

3.3.3 Temperature dependence of the Si emission

Figure 3-5 shows observed HRBS spectra of the samples annealed in 0.1 Torr O_2 for 2 min at various temperatures. Only the signals for Si and O are shown because the Hf peak did not change except for the small energy shift mentioned above. Widths of both Si and O peaks increase with increasing temperature, indicating that the thickness of the interfacial SiO_2 layer increases with annealing temperature. The yield of the surface Si also increases with increasing temperature, showing that there is a strong correlation between the growth of the interfacial SiO_2 layer and the SiO_2 overlayer. This strongly suggests that the origin of the surface Si is the Si emission from the SiO_2/Si interface during the growth of the interfacial SiO_2 layer.

There are, of course, other possibilities, e.g. the heating itself may cause the surface accumulation of Si independently of the oxidation. In order to see if this is the case, the sample was annealed in vacuum at 800°C for 2 min. The observed HRBS spectrum (a dashed line in Fig. 3-6) is very similar to the spectrum of the as-grown sample-1 (a solid line in Fig. 3-6). Neither the surface Si peak nor the growth of the interfacial layer is seen. This clearly indicates that the observed surface Si is a result of the oxidation and is not a result of the heating itself.

3.3.4 Annealing time dependence of the Si emission

Finally, we studied the annealing time dependence of the Si emission. The samples were annealed at 900°C in 0.1 Torr oxygen for various annealing times. The increase of the Si areal density of the surface SiO_2 layer, ΔD_s, and that of the interfacial SiO_2 layer, ΔD_i, were measured and the results are shown as a function of the annealing time in Fig. 3-7. The ratio of the increase of the surface Si to that of the interface Si,

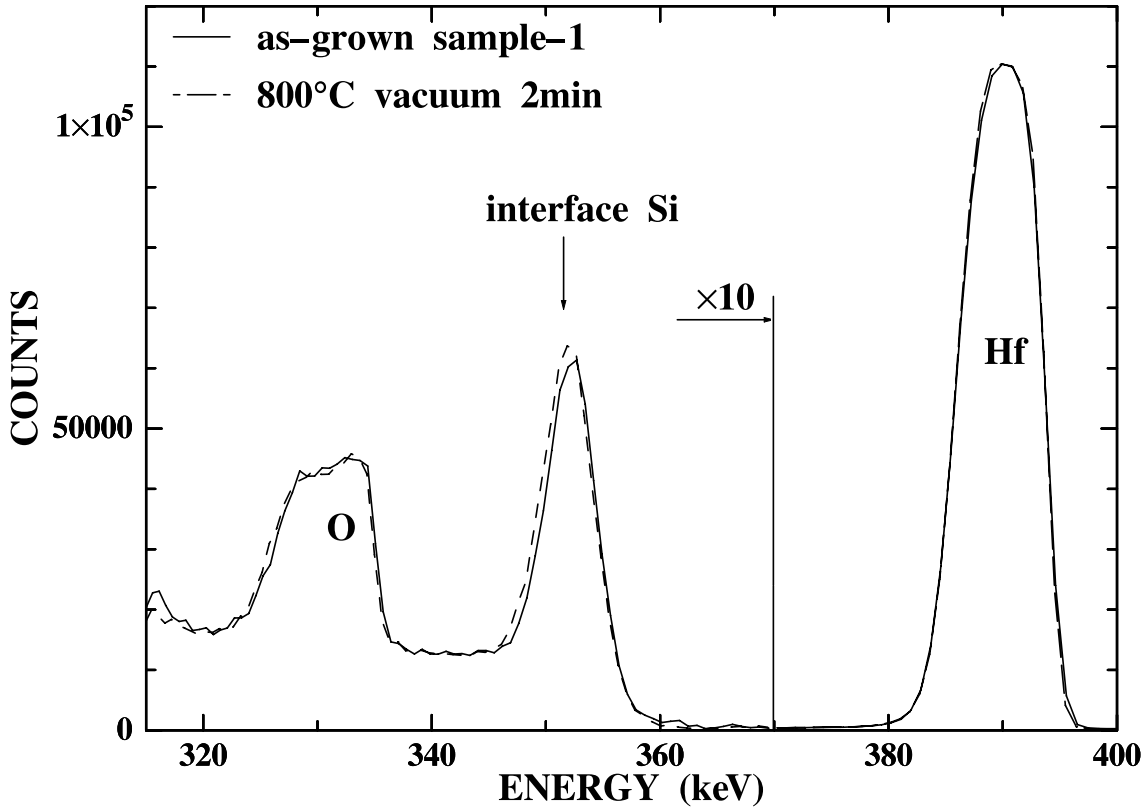

Fig. 3-6 HRBS energy spectra observed under [111] channeling conditions for the as-grown sample-1 $HfO_2/SiO_2/Si(001)$ (solid line) and the sample annealed at 800°C for 2 minutes in vacuum (dashed line). The incident ion was 400 keV He^+ and the angle of incidence and the scattering angle were 54.74° and 50°, respectively.

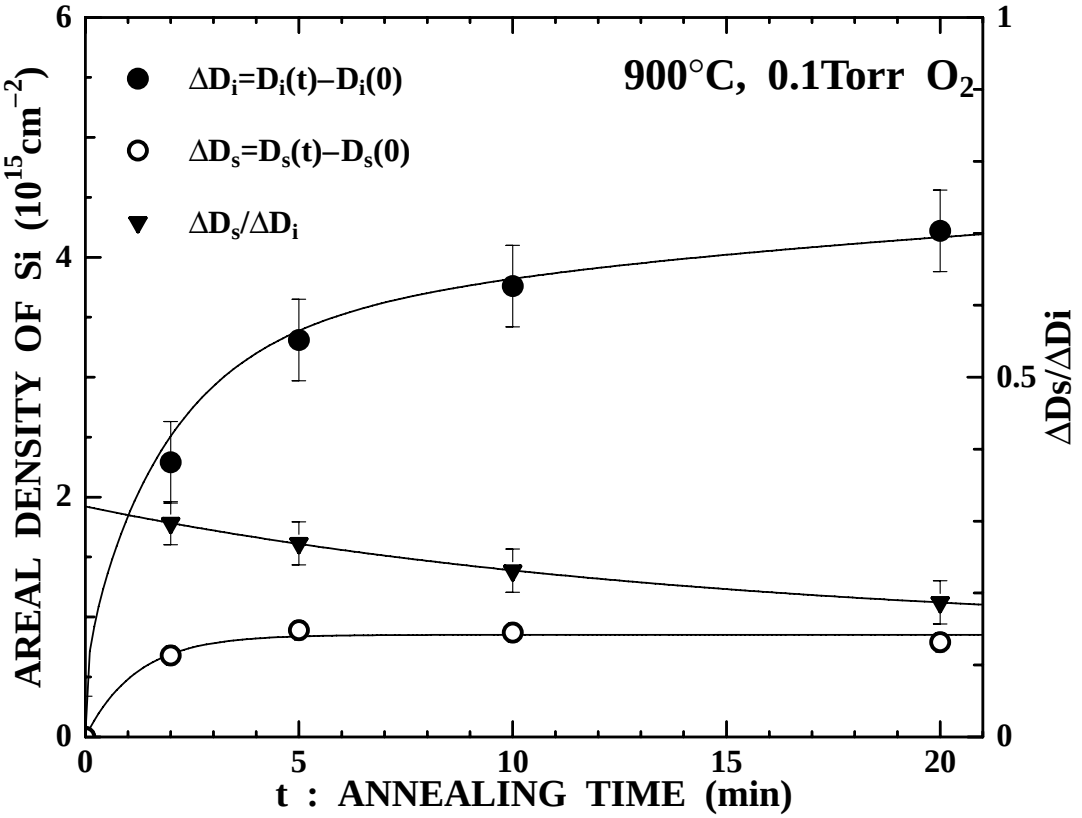

Fig. 3-7 The change of the Si areal density for the interfacial SiO_2 layer (●) and that for surface SiO_2 layer (○) for the samples after annealing at 900°C in 0.1 Torr O_2. The ratio (▼) of the latter to the former is also shown.

$\Delta D_s/\Delta D_i$, is also shown to clear up their quantitative relation.

The interfacial SiO_2 layer increases with increasing annealing time. This growth rate slows down when the annealing time exceeds 5 minutes. The surface Si also increases with annealing time but saturates after 5 minutes with the thickness of ~0.15 nm. The ratio, $\Delta D_s/\Delta D_i$, is about 0.3 at an annealing time of 2 min. This means that more than 23% (= 0.3/1.3) of Si atoms are emitted from the SiO_2/Si interface during oxidation. This is in good agreement with the result of the first principles calculation, which showed that one Si atom is kicked out of the SiO_2/Si interface when every three Si atoms are oxidized [11]. The observed ratio, $\Delta D_s/\Delta D_i$, decreases with increasing annealing time, indicating that a part of emitted Si atoms are incorporated in the interfacial SiO_2 layer. After 5 min the surface Si does not increase while the interfacial SiO_2 layer still grows. This means that the emitted Si species are almost completely incorporated in the interfacial SiO_2 layer and cannot reach the surface when the thickness of the SiO_2 layer exceeds ~ 2 nm in the present conditions (900°C in 0.1 Torr oxygen).

3.4 Conclusions

The growth of the interfacial SiO_2 layer and the simultaneous surface accumulation of Si were observed when HfO_2/SiO_2/Si was annealed in oxygen. A strong correlation was found between the growth of the interfacial SiO_2 layer and the Si surface accumulation. The observed result indicates that silicon species are emitted from the SiO_2/Si interface during the growth of the interfacial SiO_2 layer to release the stress which is induced by oxidation. The fraction of the emitted Si was estimated to be more than 23%, which is in consistent with the recent theoretical studies.

References

[1] R.M.C. de Almeida, I.J.R. Baumvol, Surf. Sci. Rep. **49**, 1(2003).

[2] G.D. Wilk, R.M. Wallace, J.M. Anthony, J. Appl. Phys. **89**, 5243(2001).

[3] B.E. Deal, A.S. Grove, J. Appl. Phys. **36**, 3770(1965).

[4] N.F. Mott, Philos. Mag. B **55**, 117(1987).

[5] R. H. Doremus, J. Mater. Res. **16**, 185(2001).

[6] K.Tatsumura, T.Shimura, E.Mishima, K.Kawamura, D.Yamasaki, H.Yamamoto, T.Watanabe, M. Umeno, I. Ohdomari, Phys. Rev. B **72**, 045205(2005).

[7] E. P. Gusev, H. C. Lu, T. Gustafsson and E. Garfunkel, Phys. Rev. B **52**, 1759 (1995).

[8] C.H. Bjorkman, J.T. Fitch, G. Lucovsky, Appl. Phys. Lett. **56**, 1983(1990).

[9] R. H. Doremus, J. Appl. Phys. **66**, 4441(1989).

[10] H.Kageshima, K.Shiraishi, Phys. Rev. Lett. **81**, 5936(1998).

[11] H.Kageshima, K. Shiraishi, Appl. Surf. Sci. **130-132**, 176(1998).

[12] H.Kageshima, K.Shiraishi and M.Uematsu, Jpn. J. Appl. Phys. **38**, L971(1999).

[13] Y. Takakuwa, M. Nihei, N. Miyamoto, Jpn. J. Appl. Phys. **32**, L480 (1993).

[14] Y. Takakuwa, M. Nihei, N. Miyamoto, Appl. Surf. Sci. **117/118**, 141 (1997).

[15] H. Watanabe, Appl. Phys. Lett. **78**, 3803 (2001).

[16] S. Sayan, E. Garfunkel, T Nishimura, W.H.Schulte, T. Gustafsson, G.D.Wilk, J. Appl. Phys. **94**, 928(2003).

[17] S. Kamiyama, T. Miura, and Y. Nara,, Appl. Phys. Lett., Vol. 87, 132904, (2005).

[18] K. Kimura, S. Joumori, Y. Oota, K. Nakajima and M. Suzuki, Nucl. Instr. and Methods B **219-220**, 351(2004).

[19] T. L. Alford, L. C. Feldman, J. W. Mayer, Fundamentals of Nanoscale Film Analysis, Springer, United States(2007).

[20] N. Miyata, Y. Morita, T. Horikawa, T. Nabatame, M. Ichikawa and A. Toriumi, Phys. Rev. B **71**, 233302 (2005).

Chapter 4

Isotopic labeling study of the oxygen diffusion in $HfO_2/SiO_2/Si$

Abstract

The characteristic oxygen diffusion in $HfO_2/SiO_2/Si$ structure during the annealing in oxygen has been investigated by high-resolution Rutherford backscattering spectroscopy in combination with oxygen isotope substitution at 900 ºC in 0.1 Torr $^{18}O_2$. While a flat distribution of ^{18}O was observed in the HfO_2 layer, the observed ^{18}O concentration decreases rapidly with depth in the SiO_2 layer and ^{18}O does not reach the SiO_2/Si interface. This result indicates that oxygen molecules are decomposed into atomic oxygen in the HfO_2 layer and the produced oxygen atoms diffuse through the oxide layer via exchange mechanism. This is also supported by the observed activation energy of ~ 0.6 eV for the growth of the SiO_2 layer.

4.1 Introduction

In the future complementary metal-oxide-semiconductor (CMOS) devices with equivalent oxide thicknesses (EOT) below 1.2 nm, SiO_2 cannot be used as gate dielectrics because of its high leakage current due to direct tunneling through such an ultra-thin film. Alternative materials with a dielectric constant higher than SiO_2, called high-*k* materials, have been extensively studied. Among these high-*k* materials, Hf based materials are most promising [1]. Compared to SiO_2, all the other dielectric materials lead to the formation of a higher density of electronic defects, such as Si dangling bond, near the Si/dielectrics interface, resulting in poor electrical properties [2]. Thus, much of the effort toward replacement of SiO_2 has been focused on stack structures, composed of an ultra-thin SiO_2 buffer underneath a high-*k* dielectric film. In current transistor process flows, gate stacks have to be exposed to temperatures as high as 1050 °C. The SiO_2 buffer layer grows during the thermal processing, and this influences the EOT [3-5]. Therefore, understanding the detailed influence of the thermal processing is important for the application of the stack structure in the future CMOS devices.

Many reports that investigated the thermal stability of $HfO_2/SiO_2/Si$ or $ZrO_2/SiO_2/Si$ structure mentioned the unusual SiO_2 growth characteristic when the stack structures were annealed in oxygen [6, 7]. Compared to the bare silicon oxidation, the initial growth rate of the SiO_2 layer in such stack structures is much faster, suggesting that HfO_2 and ZrO_2 films behave like a catalyst for SiO_2 growth. This rapid growth is significantly suppressed with increase of SiO_2 thickness. The SiO_2 thickness eventually saturates after a certain annealing time (e.g. after 5 min at 500°C and at an oxygen pressure 0.3 – 8.5 Torr [8]).

Because HfO_2 and ZrO_2 are known to be good ionic conductors of oxygen ions, it is believed that HfO_2 and ZrO_2 films decompose molecular oxygen into atomic oxygen ions and the produced oxygen ions diffuse through the HfO_2 and ZrO_2 films. The atomic oxygen is a more reactive oxidant than the molecular oxygen. As a result, the growth rate of SiO_2 could be enhanced as was observed. This scenario is supported by a recent theoretical study on the oxygen incorporation and diffusion mechanisms in HfO_2. The first-principles calculation demonstrates that oxygen favors atomic incorporation and its interstitial diffusion via exchange process has a small diffusion barrier of 0.3 eV (O^- species) in HfO_2 [9]. However, there is no clear experimental evidence for this scenario.

In the present work, we used $^{18}O_2$ as a tracer to investigate the diffusing characteristic of oxygen in $HfO_2/SiO_2/Si$ structure during thermal processing. The influence of HfO_2 on oxygen diffusing and SiO_2 growth is discussed.

4.2 Experimental

Several pieces of the as-grown sample-1 were annealed in an infrared furnace (MLLA 3000) at 500-900°C in 0.1 Torr dry $^{18}O_2$ or $^{16}O_2$ for 30 s - 20 min.

These samples were observed by HRBS [10] using 400 keV He^+ ions as a probe. The details of the HRBS measurement were described in Chapter 2. In the present measurements, samples were aligned to a channeling configuration with the [111] or [211] axis parallel to the incident beam, reducing the silicon substrate contribution, which helps us to analyze the oxygen signal precisely. Energy spectra of He^+ ions scattered at 50° or 75° were measured by a 90° sector magnetic spectrometer.

4.3 Results and discussion

4.3.1 Growth of the interfacial SiO_2

Figure 4-1 shows HRBS energy spectra observed at a scattering angle of 50° under the [111] channeling condition. The spectra of samples annealed in 0.1 Torr $^{16}O_2$ at 900°C for various times are shown. Only the signals for Si and O are shown because Hf spectrum did not change under the present annealing conditions.

A large peak seen at ~330 keV corresponds to oxygen in both the HfO_2 and SiO_2 layers. A broad peak at ~350 keV corresponds to Si in the SiO_2/Si interface region. The yields of O and Si interface peak increase with annealing time. The Si interface peak consists of contributions from the interfacial SiO_2 layer and the substrate Si atoms which can be seen by the channeling ions. The latter contribution mainly comes from the topmost Si atomic layer in the substrate and is almost independent of the thickness of the interfacial SiO_2 unless the SiO_2 layer is extremely thick. Therefore, the observed increment of the Si interface peak yield is attributed to the growth of the SiO_2 layer, and the thickness of the SiO_2 interface layer can be estimated from the Si interface peak. A small peak appeared around 361 keV in the spectra of annealed samples corresponds to Si that out-diffusing to the surface during the Si substrate oxidation, which has been discussed in Chapter 3.

Figure 4-2 shows the obtained results of the SiO_2 interface layer thickness as a function

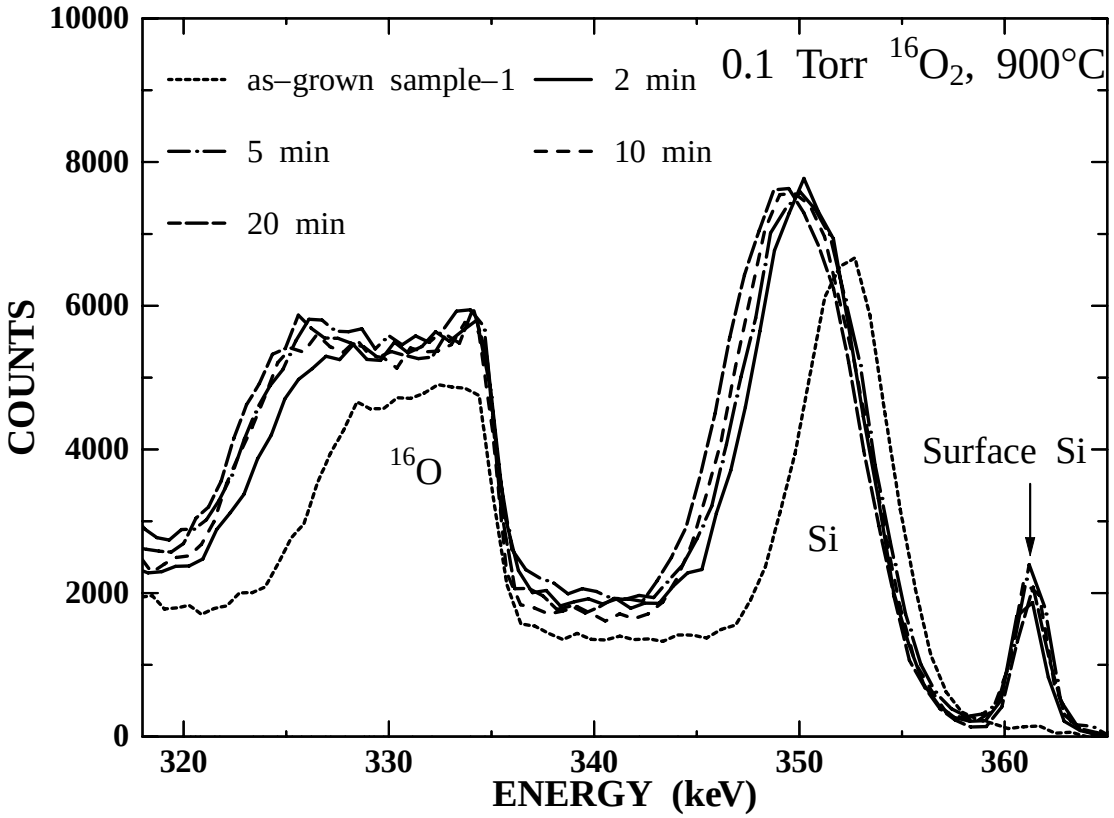

Fig. 4-1 HRBS energy spectra observed under [111] channeling conditions for as-grown sample-1 $HfO_2/SiO_2/Si$ (dot line) and samples annealed in 0.1 Torr O_2 at 900°C for various time; 2 min (solid line), 5 min (long dashed line), 10 min (short dashed line), 20 min (dashed line). The incident ion was 400 keV He^+ and the angle of incidence and the scattering angle were 54.74° and 50°, respectively.

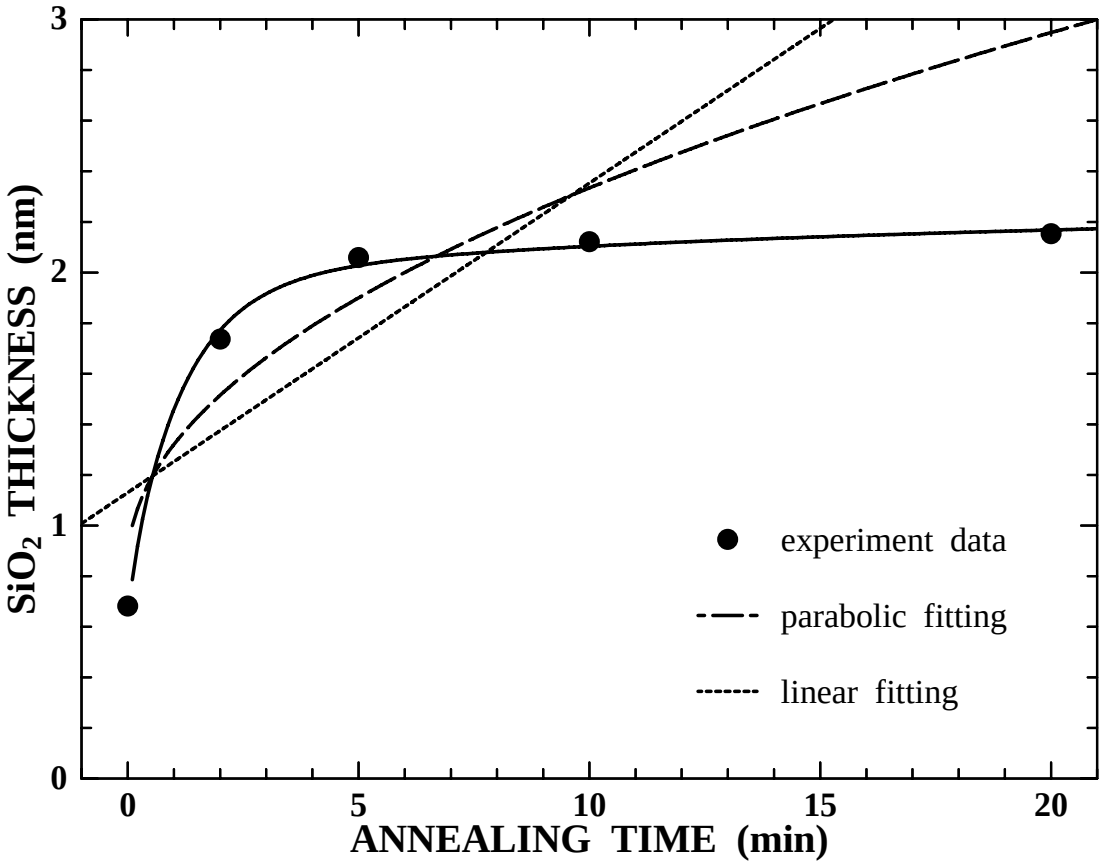

Fig.4-2 Estimated results of SiO_2 thickness vs. annealing time based on the data of Fig. 4-1. The solid line is for the guidance only. Dot line and dashed line is the linear and parabolic fitting according to Deal-Grove model, respectively.

of annealing time. The black dots represent the experimental data and the solid line is for guidance only. The dashed line shows the result of parabolic fitting and the dot line shows that of the linear fitting. It is clear that the growth of SiO_2 follows neither the linear law nor the parabolic law which were predicted by the Deal-Grove model. The growth rate is impressively large before the SiO_2 thickness is ~2 nm. The observed growth rate is 0.5 nm/min in the first 2 min. It is 5 times larger than the reported oxidation rate for 0.7 nm SiO_2 atop Si at the same temperature and in a higher oxygen pressure [11]. Such a kind of initial acceleration of SiO_2 growth has been reported when $HfO_2/SiO_2/Si$ [12] or $ZrO_2/SiO_2/Si$ [13] samples were annealed in the oxygen ambient. After the initial enhanced growth, however, the growth rate decreases very rapidly and no more growth was observed after 10 min. This growth rate character reminds one the oxidation of silicon by O or O^- species without external bias [14-17].

4.3.2 Isotopic tracing

In order to clarify the origin of the enhancement of SiO_2 growth rate, the behavior of oxygen during the annealing was observed using ^{18}O as a tracer. The $HfO_2/SiO_2/Si$ (001) structure was annealed at 900°C in 0.1 Torr static $^{18}O_2$ for 2 minutes. HRBS spectra were measured at a scattering angle of 75° under the [211] channeling condition before and after the annealing. The scattering condition was chosen to separate the ^{18}O signal from ^{16}O.

Figure 4-3 shows the HRBS energy spectra observed before and after oxidation in $^{18}O_2$. The ^{18}O peak can be seen at ~ 280 keV. Figure 4-4 shows the composition profile of the as-grown sample-1 and the annealed sample obtained after a simulation of the HRBS spectrum. The simulated spectra are shown by the solid lines in Fig. 4-3.

The flat profile of ^{18}O in HfO_2 seen in Fig. 4-4(b) indicates that the oxygen diffusion in HfO_2 layer achieved to an equilibrium condition within 2 min under the current condition. The result represents an extremely high diffusion coefficient of oxygen in HfO_2. This is consistent with the previous report [18] and indicates that the diffusing of oxygen in HfO_2 is not the rate limiting step of the Si oxidation.

More detailed inspection of the ^{18}O profile in the SiO_2 layer reveals that ^{18}O exists only near the HfO_2/SiO_2 interface. The result of the simulation that assumed ^{18}O went all the way through SiO_2 layer is shown by dash line in Fig.4-3. Apparently, the simulated spectrum shown by solid line is in better agreement with the experimental

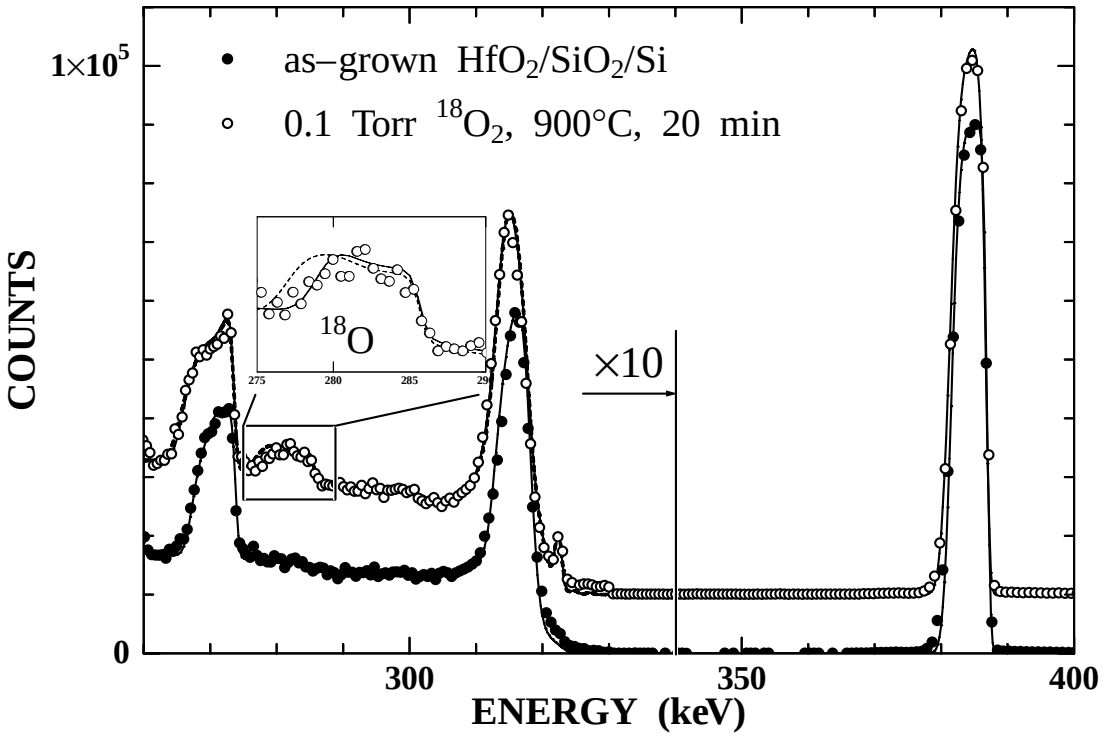

Fig. 4-3 HRBS spectra observed under [211] channeling conditions for as-grown sample-1 $HfO_2/SiO_2/Si$ (lower spectrum) and a sample annealed in 0.1 Torr $^{18}O_2$ at 900°C for 20 min (upper spectrum). The results of simulation are also shown by solid lines. The incident ion was 400 keV He^+, and the angle of incidence and the scattering angle were 54.74° and 75°, respectively.

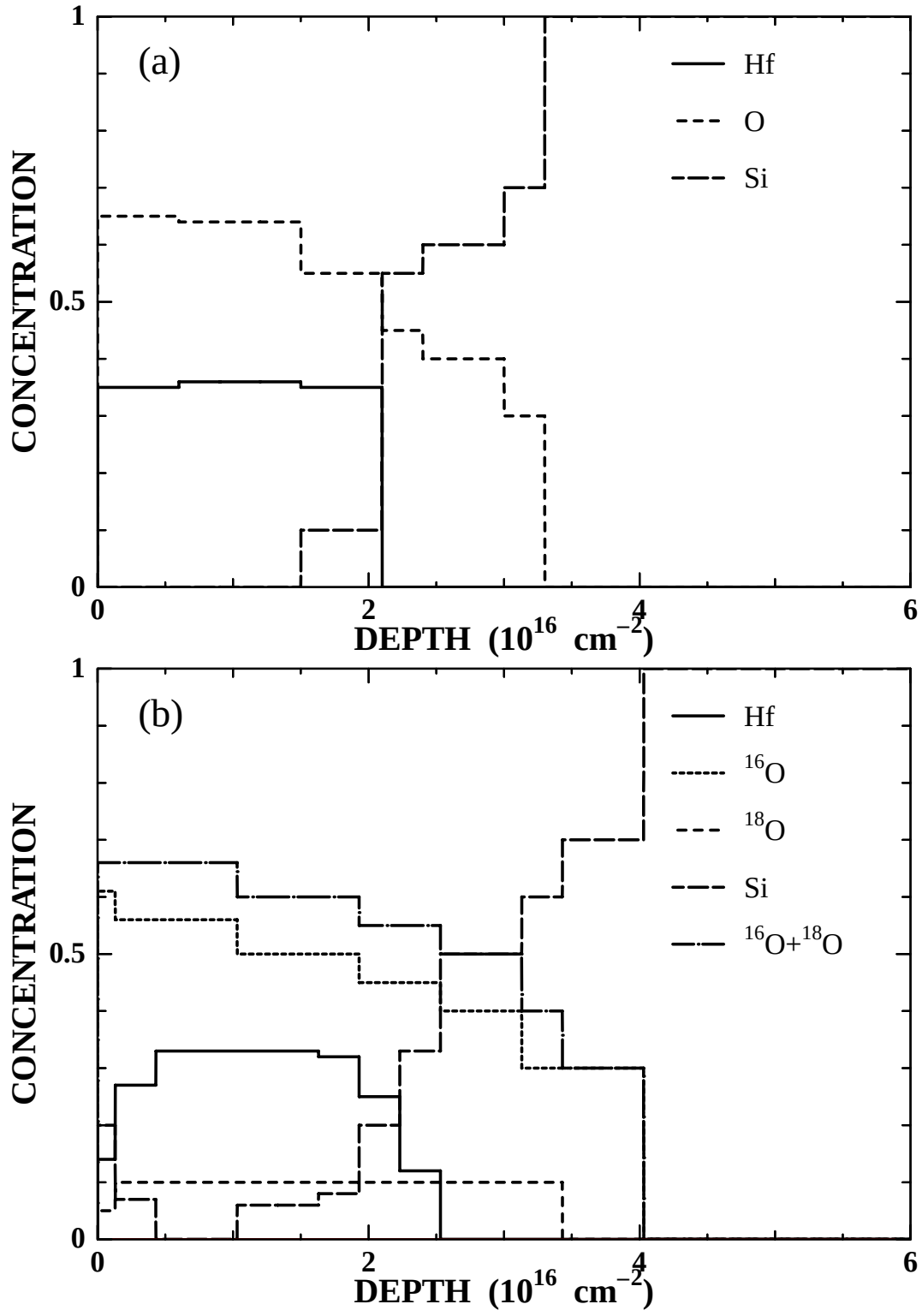

Fig. 4-4 Depth profiles of elements in the as-grown sample-1 (a) and the sample annealed in 0.1 Torr $^{18}O_2$ at 900°C for 20 min (b).

spectrum, which confirms that ^{18}O exists only near the HfO_2/SiO_2 interface in the SiO_2 layer. This phenomenon is quite different from the ^{18}O distribution in SiO_2/Si structure oxidized by $^{18}O_2$, which usually shows an accumulation of ^{18}O near the SiO_2/Si interface whenever the interfacial SiO_2 layer increment was observed [19-21]. In that case, molecular oxygen is the dominant diffusing oxidant and easily diffuses through the SiO_2 network. If oxygen molecule is the dominant diffusing species in HfO_2, the accumulation of ^{18}O at SiO_2/Si interface should be observed. The completely different depth profile observed here indicates that oxygen molecule is not the dominant diffusing species in HfO_2. Atomic oxygen, either O or O^-, seems to be the most reasonable diffusing oxidant in HfO_2 under the current condition (900°C, 0.1Torr O_2).

There are two possible mechanisms of diffusion of atomic oxygen in oxide, the interstitial mechanism and exchange mechanism. In the interstitial mechanism, the interstitial oxygen atoms diffuse through empty space between the lattice sites without reaction with the oxide network. If this is the case in the SiO_2 layer, ^{18}O should distribute at the SiO_2/Si interface region where the oxidation reaction happens. On the other hand, the exchange mechanism involves the continuous replacement of a lattice site by the diffusing defect, and the lattice site then becoming the diffusing species. This mechanism is traditionally known as the "Interstitialcy" mechanism. It is characteristic of diffusion of anions, for example, in MgO [22]. In this mechanism, incorporated ^{18}O atoms push the already existing ^{16}O toward SiO_2/Si interface. The present ^{18}O profile is consistent with the result expected from the exchange mechanism. This result indicates that atomic oxygen interstitials diffuse via exchange mechanism in SiO_2.

4.3.3 Temperature dependence of the growth rate of the interfacial SiO_2 layer

Figure 4-5 illustrates the observed initial growth rate of SiO_2 in the first 2-min annealing on a logarithmic scale versus $1/k_BT$ corresponding to the annealing temperature of 500 ~ 900°C. The SiO_2 thicknesses of these samples after 2-min annealing are all less than 2 nm. The observed growth rate shows an Arrhenius dependence on the annealing temperature. The solid line is the result of the linear fitting to the experimental data points. The obtained activation energy is ~0.6 eV. Because the diffusion of oxygen in HfO_2 is not the rate limiting process in the present case as was mentioned above, this activation energy should be related to the oxygen diffusion in SiO_2 and/or oxygen reaction with Si at SiO_2/Si interface.

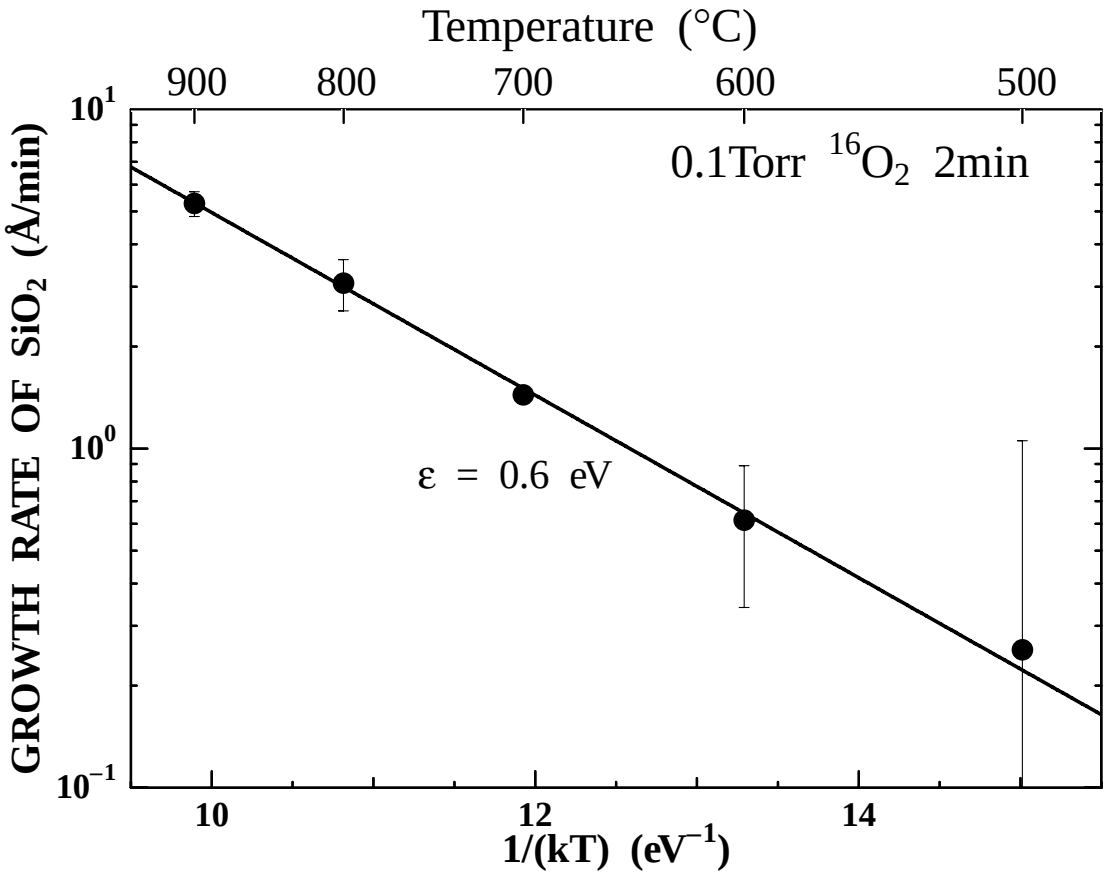

Fig. 4-5 Logarithmic plot of the average growth rate of SiO_2 in $HfO_2/SiO_2/Si$ structure annealed in 0.1 Torr O_2 for 2 minutes vs. reciprocal temperature. The solid line is the linear fitting result.

The linear growth rate *B/A* in the Deal-Grove model for dry oxidation of (100) silicon has an activation energy of 1.76 eV for $T \leq 1000°C$ and 3.20 eV for $T \geq 1000°C$ [23]. Even some literature reported a higher growth rate of SiO_2 during the first 5 s, that growth rate has an activation energy of 1.21 eV [24]. The effective activation energy of SiO_2 growth rate in this work is much smaller than these values, but comparable to the reported values of diffusion activation energy of O^- in SiO_2 (0.14 ~ 0.7 eV) [25, 26], in consistent with the previous conclusion, i.e. the dominant diffusing oxygen species is atomic oxygen ions.

4.3.4 Estimation of concentration of oxygen interstitial

Because the incorporated oxygen in HfO_2 acts as the electron trap, the performance of HfO_2 as a gate dielectric film is strongly influenced by the interstitial oxygen. On the basis of the present results, the concentration of interstitial oxygen in HfO_2 during the annealing in the oxygen ambient can be estimated. Figure 4-6 is a sketch of the distribution of oxygen interstitials in $HfO_2/SiO_2/Si$. Oxygen interstitials are produced by the catalytic reaction in HfO_2 and diffuse through the HfO_2 layer via the exchange process. This procedure is so fast that the equilibrium condition is obtained very rapidly and a flat distribution of oxygen interstitials is achieved immediately in HfO_2 as was observed. We assume that the active oxygen concentration on the SiO_2/Si interface is zero, that is to say the reaction of silicon with oxygen is not the rate limiting step of SiO_2 growth. Using these assumptions, the increased amount of oxygen in the grown SiO_2 layer is calculated as follows:

$$\Delta N_{ox} = D_O \cdot \frac{C_{eq}}{d_{ox}} \cdot t \,, \tag{4-1}$$

where D_o is the diffusion coefficient of the interstitial oxygen in SiO_2, which was reported to be 1.8×10^{-8} cm^2/s at 900°C [29], C_{eq} is the balance concentration of oxygen interstitials in the HfO_2 under the equilibrium condition, d_{ox} is the SiO_2 thickness and t is the annealing time. Substituting the observed values for the 2 min-annealing at 900 °C, $\Delta N_{ox} = 5 \times 10^{15}$ cm^{-2}, t = 120 sec, and d_{ox} = 1.2 nm (observed average thickness during the 2-min annealing), into Eq. (4-1), C_{eq} is estimated to be $\sim 3 \times 10^{14}$ cm^{-3}.

Finally we note that the initial enhancement of the SiO_2 growth rate is suppressed after the interfacial SiO_2 layer becomes thicker. In the initial stage of the interfacial SiO_2 growth, HfO_2 behaves as a catalyst because it provides reactive oxidants, i.e. atomic oxygen. But atomic oxygen has a characteristic diffusing length in SiO_2, through which area the atomic oxygen will combine into molecule, which is much less reactive

than the atomic oxygen. Thus, when the SiO_2 layer becomes thicker than this characteristic length, which is determined by the diffusion condition, the catalytic behavior of HfO_2 on Si oxidation disappears and the SiO_2 growth is suppressed as was observed.

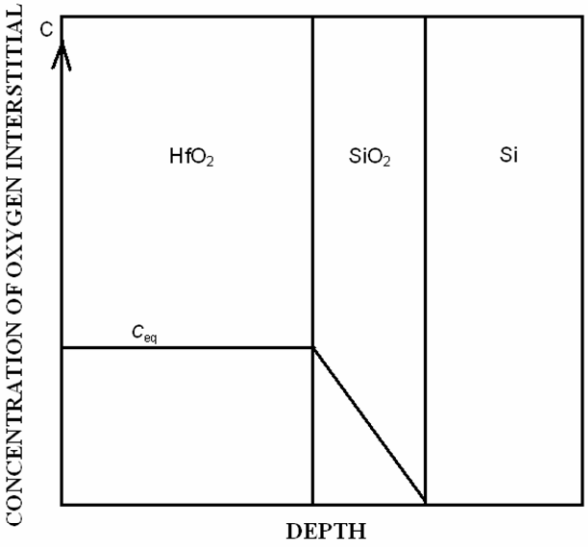

Fig. 4-6 Sketch of the concentration profile for oxygen interstitials in $HfO_2/SiO_2/Si$.

4.4 Conclusions

The ^{18}O depth profile was measured by HRBS after annealing a HfO_2(3 nm)/SiO_2(0.7 nm)/Si structure at 900 °C in 0.1Torr $^{18}O_2$. While the observed ^{18}O concentration is almost constant in the HfO_2 layer, the ^{18}O concentration decreases rapidly with depth in the interfacial SiO_2 layer. These results together with the observed activation energy ~ 0.6 eV for the growth of the interfacial SiO_2 layer indicates that oxygen molecules are decomposed into atomic oxygen in the HfO_2 layer and the produced oxygen atoms diffuse through the oxide layer via exchange mechanism. Using a simple model based on the above findings and the observed growth rate of the interfacial SiO_2 layer, the equilibrium concentration of oxygen interstitials in HfO_2 is estimated to be ~ 3×10^{14} cm^{-3} at 900°C in 0.1 Torr O_2.

References

[1] G. Lucovsky, Y. Wu, H. Niimi, V. Misra, J. C. Philips, Appl. Phys. Lett.**74**, 2005 (1999).

[2] A. Fissel, H. J. Osten, E. Bugiel, J. Vac. Sci. Technol. B **21**, 1765 (2003).

[3] G. D. Wilk, R.M. Wallace, J.M. Anthony, J. Appl. Phys. **89**, 5243(2001).

[4] A.Callegari, E. Cartier, M. Gribelyuk, H. F. Okom-Schmidt, T. Zabel, J. Appl. Phys. **90**, 6466 (2001).

[5] M. Copel, E. Cartier, T. M. Ross, Appl. Phys. Lett.**78**, 1607 (2001).

[6] N. Miyata, M. Ichikawa, T. Nabatame, T. Horikawa, A. Toriumi, Jpn. J. Appl. Phys. **42**, L138 (2003).

[7] H. Watanabe, N. Ikarashi, Appl. Phys. Lett. **80**, 559 (2002).

[8] B. W. Busch, W. H. Schulte, E. Garfunkel, T. Gustafsson, Phys. Rev. B **62**, R13290 (2000).

[9] A. S. Foster, A. L. Shluger, R. M. Nieminen, Phys. Rev. Lett. **89**, 225901 (2002).

[10] K. Kimura, S. Joumori, Y. Oota, K. Nakajima and M. Suzuki, Nucl. Instr. and Methods B **219-220**, 351 (2004).

[11] H. Z. Massoud, J. D. Plummer, E. A. Irene, J. Electrochem. Soc. **132**, 1745 (1985).

[12] Watanabe, Appl. Phys. Lett. **78**, 3803 (2001).

[13] Shih-Sian Huang and Tai-Bor Wu, J. Vac. Sci. Technol. B **22**, 2702 (2004).

[14] J. R. Ligenza, J. Appl. Phys. **36**, 2703 (1965).

[15] I. W. Boyd, V. Craciun, A. Kazor, Jpn. J. Appl. Phys. **32**, 6141 (1993).

[16] H. Itoh, M. Nagamine, H, Satake, A. Toriumi, Microelectron. Eng. **48**, 71 (1999).

[17] A.Kazor, I. W. Boyd, J. Appl. Phys. **75**, 227 (1994).

[18] S. Ferrari, G. Scarel, J. Appl. Phys. **96**, 144 (2004).

[19] E. Rosencher, A. Straboni, S. Rigo, G. Amsel, Appl. Phys. Lett. **34**, 254 (1979).

[20] T. Gustafsson, H. C. Lu, B. W. Busch, W. H. Scchulte, E. Garfunkel, Nucl. Instr. and Meth. in Phys. Res. B **183**, 146 (2001).

[21] H. C. Lu, T. Gustafsson, E.P. Gusen, E. Garfunkel, Appl. Phys. Lett. **67**, 1742 (1995).

[22] T. Brudevoll, E. A. Kotomin, N. E. Christensen, Phys. Rev. B **53**, 7731 (1996).

[23] H. Z. Massoud, J. D. Plummer, E. A. Irene, J. Electrochem. Soc. **132**, 2685 (1985).

[24] Mehrdad M. Moslehi, Steven C. Shatas, Krishna C. Saraswat, Appl. Phys. Lett. **47**, 1353 (1985).

[25] Y. Yasuda, S. Zaima, T, Kaida, Y. Koide, J. Appl. Phys. **67**, 2603 (1990).

[26] S. K. Sharma, B. C. Chakravarty, S. N. Singh, B. K. Das, J. Mater. Sci. Lett. **9**, 982 (1990).

[27] E. Gusev, C. Cabral, Jr, M. Copel, C. D. Emic, and M. Gribelyuk, Microelectron. Eng. **69**, 145 (2003).

[28] L. V. Goncharova, M. Dalponte, D. G. Starodub, T. Gustafsson, E. Garfunkel, P. S. Lysaght, B. Foran, J. Barnett, and G. Bersuker, Appl. Phys. Lett. **89**, 044108 (2006).

[29] L. Skuja, K. Kajihara, M. Hirano, H. Hosono, Abstract book of The 52nd Spring Meeting of The Japan Society of Applied Physics, 29a-ZB-5, p.888, 2005 (in Japanese).

Chapter 5

In situ observation of oxygen gettering by titanium overlayer on $HfO_2/SiO_2/Si$ using high-resolution Rutherford backscattering spectroscopy

Abstract

Oxygen-gettering by Ti overlayer (2 ~ 8 nm) on a HfO_2(3nm)/SiO_2(1.5 nm)/Si(001) structure was investigated using high-resolution Rutherford backscattering spectroscopy. After deposition of a thin Ti layer, the interfacial SiO_2 layer is reduced by ~ 0.2 nm and the released oxygen is incorporated in Ti layer. Subsequent annealing at 330 °C in UHV causes further reduction by 0.1 ~ 0.8 nm depending on the Ti layer thickness. In addition to the reduction of the SiO_2 layer, significant oxygen depletion in the HfO_2 layer was observed for thicker Ti layers after annealing.

5.1 Introduction

Beyond 65-nm design rule, the conventional SiO_2-based materials cannot be used as gate dielectrics in complementary metal oxide semiconductor (CMOS) devices because of its high leakage current due to direct tunneling. Intensive studies have been performed to search alternative materials with a higher dielectric constant. Among the various materials, HfO_2 and other Hf-based materials are most promising candidates for the gate dielectrics films in the future CMOS devices [1]. The interface between HfO_2 and Si, however, is not perfect as the SiO_2/Si interface. There are physical and electrical defects at the HfO_2/Si interface, which cause degradation of the device performance [2]. In order to solve this problem, an ultrathin SiO_2 layer is grown on Si before the formation of the HfO_2 film. In the conventional CMOS process flow, however, the dopant drive-in anneal at ~1000 ºC is necessary. This annealing causes growth of the interfacial SiO_2 layer and consequently increase of the equivalent oxide thickness (EOT) and the degradation of the device performance [3 – 5]. Accordingly, the control of the interfacial SiO_2 layer is an important issue. Recently, Kim *et al* observed effective removal of the interfacial SiO_2 layer by deposition of Ti layer on HfO_2/SiO_2/Si(001) and subsequent annealing at 300 ºC using TEM [6]. This could be a promising technique to control the interfacial SiO_2 layer. To this end, however, more detailed understanding of the oxygen-gettering process is indispensable.

In the present work, we observe the oxygen-gettering process *in situ* using high-resolution Rutherford backscattering spectroscopy (HRBS). We found that the SiO_2 layer is reduced by ~ 0.2 nm just after the deposition of the Ti overlayer irrespective of the Ti layer thickness. A further reduction was observed after annealing at 330 °C and the amount of the reduction depends on the thickness of the Ti overlayer. We also found considerable oxygen depletion up to ~ 50% in the HfO_2 layer after annealing with thicker Ti layers.

5.2 Experimental

A HfO_2 film of ~ 3 nm thickness was grown by atomic layer deposition (ALD) using tetrakis (ethylmethylamino) hafnium $\{Hf[N(CH_3)(C_2H_5)]_4\}$ with O_3 as an oxidant after preparing a SiO_2 layer of 0.7 nm thickness on Si(001) [7]. After deposition of HfO_2, the sample was annealed in 1 Torr O_2 at 1000 °C for 10 sec. During the annealing the interfacial SiO_2 layer grew to ~ 1.5 nm. The sample thus prepared (as-grown sample-2) was mounted on a goniometer in UHV chamber (base pressure 4×10^{-10} Torr)

and heated up to ~ 200 °C for one day to remove the molecules adsorbed on the surface. After cooling down to the room temperature Ti was deposited on the $HfO_2/SiO_2/Si(001)$ by resistive heating of Ti wire (purity 99.9%). Thin Ti layers of three different thicknesses, 1.8, 3.6, 7.9 nm, were grown and annealed at 330 °C for 30 min in the chamber.

During these processes, the samples were observed *in situ* by HRBS using 400 keV He^+ ions as a probe. The details of the HRBS measurement were described elsewhere [8]. Briefly, energy spectra of He^+ ions scattered at 75° were measured by a 90° sector magnetic spectrometer. In addition to the so-called random spectra, channeling spectra were measured to reduce the Si substrate signal. This allows precise measurements of oxygen.

5.3 Results and discussion

5.3.1 Oxygen getting by Ti deposition

Figure 5-1 shows the HRBS spectra observed under [113] channeling conditions. The solid line shows the spectrum of the as-grown sample. There are three peaks in the spectrum. The largest peak at ~ 390 keV corresponds to Hf in the HfO_2 layer. The peak at ~ 310 keV is mainly attributed to Si in the SiO_2 layer and the peak at ~ 260 keV corresponds to oxygen in both HfO_2 and SiO_2 layers.

After deposition of a Ti layer of 3.6 nm thickness, these peaks shift toward lower energies and a new peak appears at ~ 350 keV, which corresponds to the Ti layer (see the spectrum shown by open circles). More detailed inspection of the spectrum revealed that the oxygen peak has a tail towards higher energies. This indicates that some oxygen atoms diffused into the Ti layer during the Ti deposition. The closed circles show the HRBS spectrum observed after annealing at 330 °C for 30 min. It is clearly seen that the shape of the oxygen peak changes drastically, indicating that a large amount of oxygen moves toward shallower region. In addition, the Ti peak becomes broader. These changes indicate that oxygen atoms are incorporated in the Ti layer. To see the behavior of oxygen in detail, elemental depth profiles were derived from the observed HRBS spectra.

Figure 5-2(a) shows the derived depth profiles for the as-grown sample-2 (before Ti deposition). The twice of the Hf concentration is also shown by a dashed curve. Except for the interface region the dashed curve agrees with the oxygen profile very

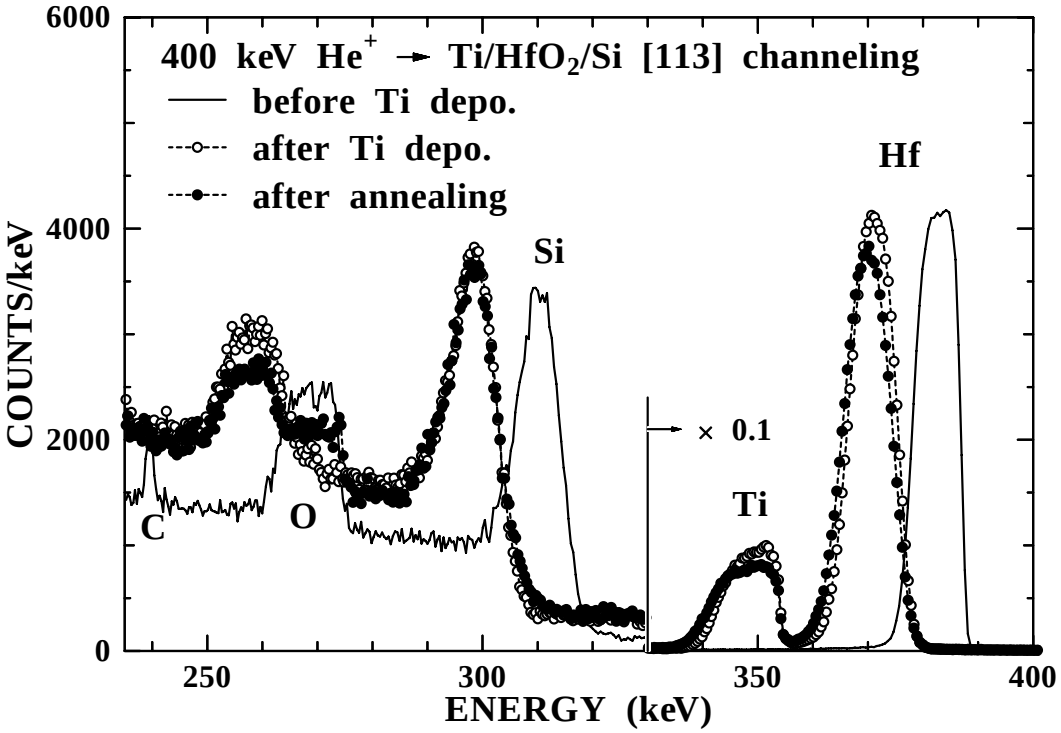

Fig. 5-1 HRBS energy spectra observed under [113] channeling conditions for the as-grown sample-2 $HfO_2/SiO_2/Si(001)$ (solid line), after Ti deposition of 3.6 nm at RT (○) and after successive annealing at 330 °C for 30 min in UHV (●).

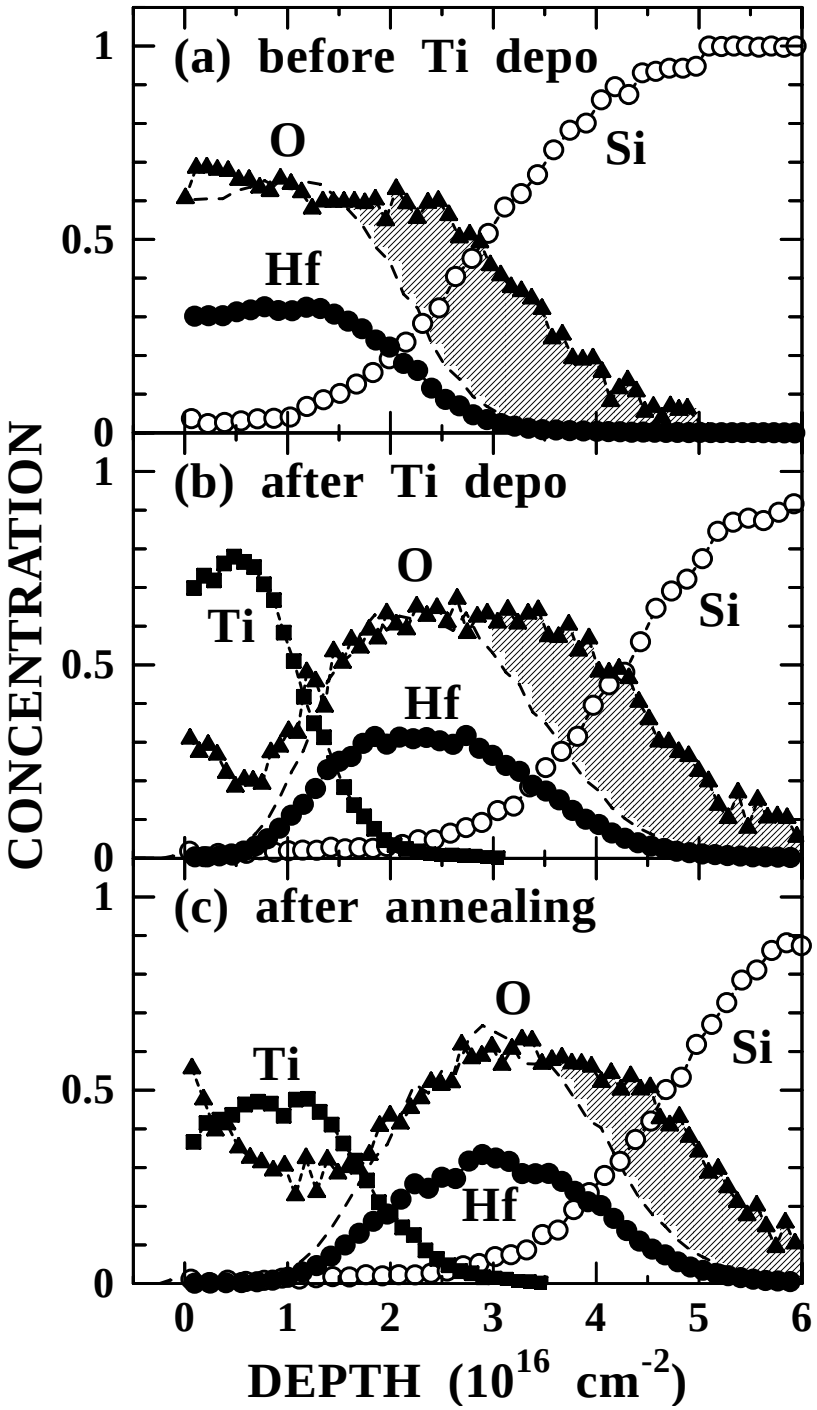

Fig. 5-2 Elemental depth profiles for (a) as-grown sample-2 $HfO_2/SiO_2/Si(001)$ (solid line), (b) after Ti deposition of 1.8 nm at RT and (c) after successive annealing at 330 °C for 30 min in UHV. The dashed curve shows the twice of the Hf concentration.

well. This indicates that a stoichiometric HfO_2 layer was prepared. The thickness of the HfO_2 layer is estimated to be 2.2×10^{16} atoms/cm^2, which corresponds to 2.8 nm (ρ = 9.7 g/cm^3 is used). In the interface region ($d \sim 3 \times 10^{16}$ atoms/cm^2), there are extra oxygen atoms forming a SiO_2 layer (shaded area). From the observed yield of the extra oxygen, the thickness of the interfacial SiO_2 layer was estimated to be 1.5 nm.

After deposition of a 1.8 nm Ti layer, the extra oxygen in the interface region becomes smaller, indicating that the interfacial SiO_2 layer is reduced (Fig. 5-2(b)). The oxygen released from the SiO_2 layer is incorporated in the Ti layer. The oxygen concentration is close to the solubility limit in Ti (34 at. % [9]). After annealing at 330 °C for 30 min, the reduction of the SiO_2 layer can be seen more clearly and further oxygen incorporation in the Ti layer is also seen, while the stoichiometry of the HfO_2 layer is not changed (see Fig. 5-2(c)). It should be noted that, in the interface region, the profiles of Hf, Si and O do not change their shape and the profiles are just shifted. This means that the composition of the interfacial SiO_2 layer is not changed but just the thickness is reduced.

5.3.2 The thickness of Ti layer influence on the oxygen getting amount

Figure 5-3 shows the change of the SiO_2 layer thickness due to the Ti deposition and annealing for three different Ti overlayers of 1.8, 3.6 and 7.9 nm. The reduction of the SiO_2 layer due to the Ti deposition is about 0.2 nm and this reduction does not depend on the thickness of the Ti layer within the experimental error. The additional reduction due to the annealing, however, increases with thickness of the Ti layer. The thickness of the SiO_2 layer was reduced down to 0.5 nm after annealing in the case of the thickest Ti layer (7.9 nm). The present result shows that the oxygen-gettering by Ti is a promising technique to control the thickness of the interfacial SiO_2 layer. There is, however, a serious flaw for this technique.

Figure 5-4 shows the depth profiles observed before and after annealing for a thick Ti overlayer (7.9 nm). Considerable reduction of oxygen concentration in HfO_2 layer is seen after annealing although the remaining SiO_2 layer still exists. The reduction of oxygen concentration is almost 50% after annealing. This might be surprising because it is energetically more favorable for oxygen to from HfO_2 rather than SiO_2. The present observation suggests that SiO_2 becomes patchy and discontinuous in the final stage of destruction.

Recent XPS study on the oxygen-gettering by Ti overlayer (50 nm) on $HfO_2/SiO_2/Si$

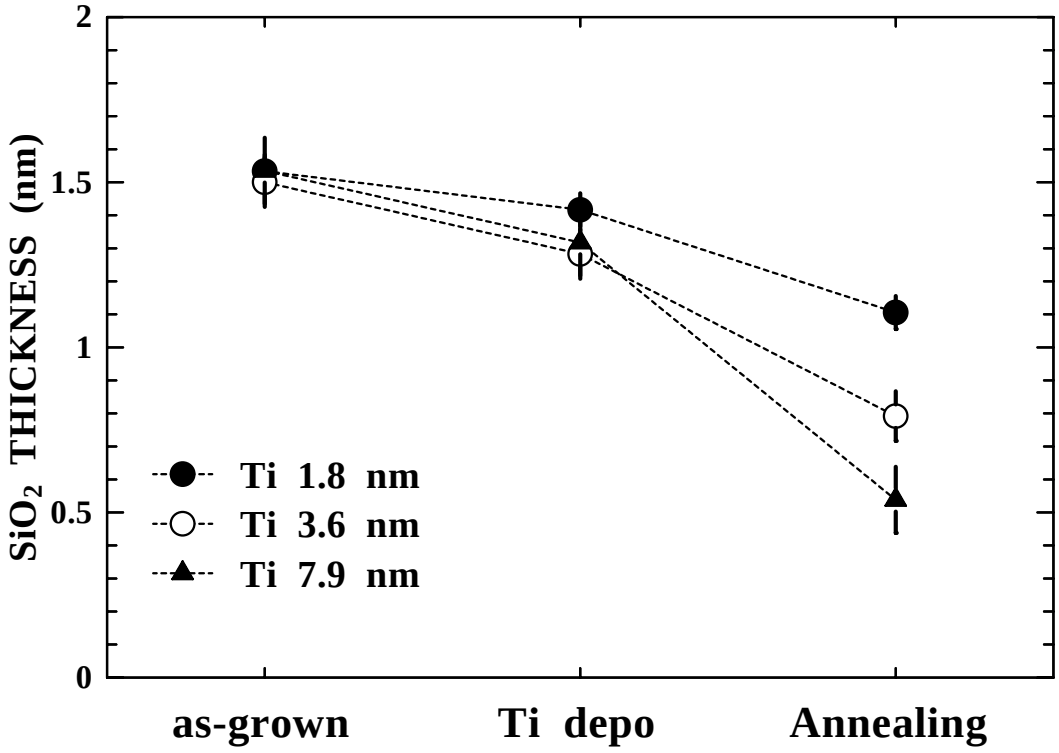

Fig. 5-3 Change of thickness of the interfacial SiO_2 layer. Results for three different Ti layer thicknesses (1.8, 3.6 and 7.9 nm) are shown. While the reduction of the SiO_2 layer due to Ti deposition does not depend on the Ti layer thickness, the reduction due to annealing increases with Ti layer thickness.

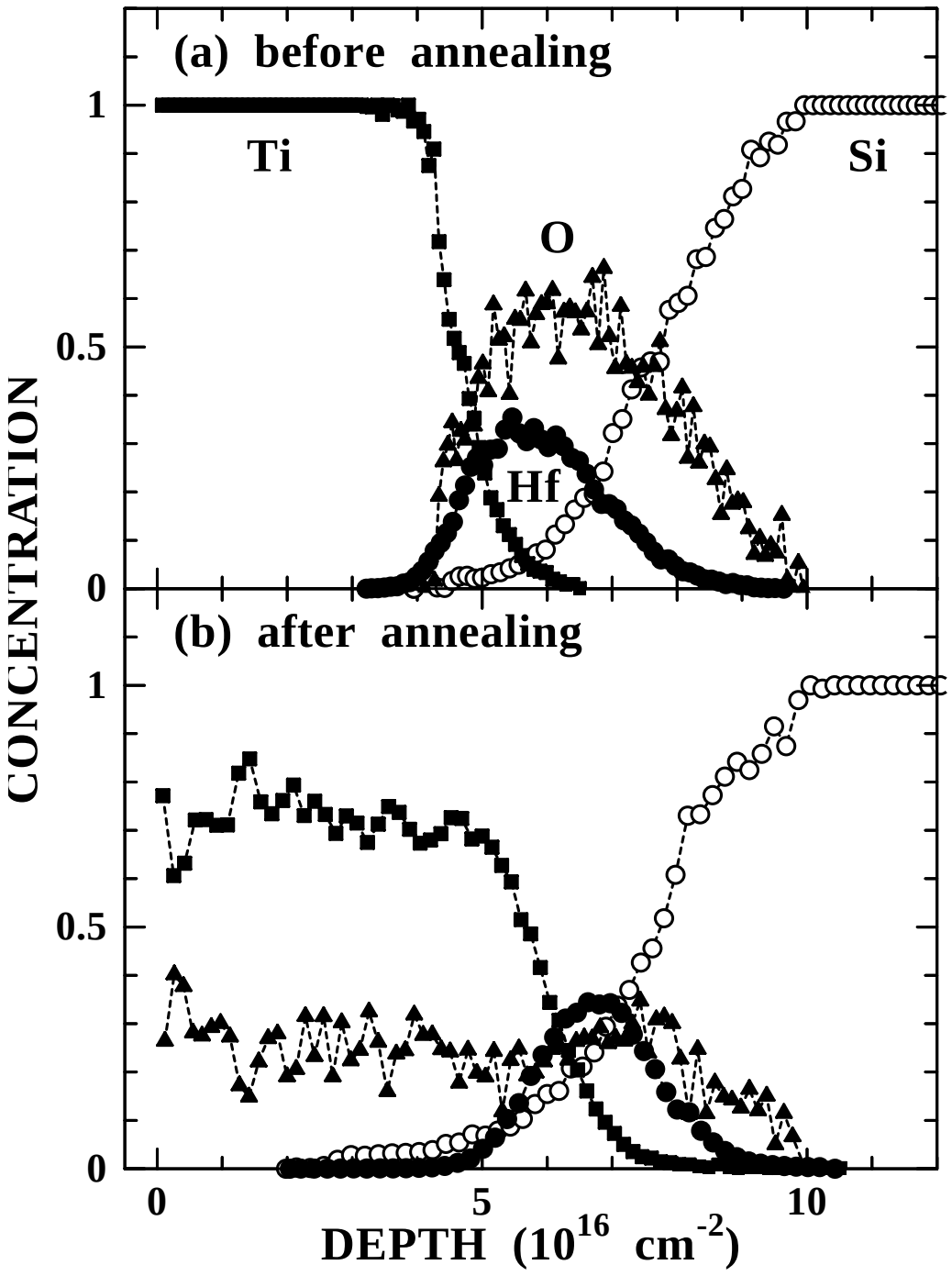

Fig. 5-4 Elemental depth profiles in Ti(7.9 nm)/HfO_2/SiO_2/Si(001) observed (a) before and (b) after annealing at 330 ºC for 30 min in UHV.

showed a signature of silicate formation at the HfO_2/SiO_2 interface but no evidence was reported for the oxygen depletion in the HfO_2 layer [10]. They annealed $Ti/HfO_2/SiO_2/Si$ in a forming gas (4% H_2/96% N_2) at 300 °C and removed both Ti and HfO_2 layers by 30 wt % H_2O_2 solution and a dilute HF solution before XPS measurement, while we measured HRBS spectra *in situ* without breaking vacuum. The different result observed by XPS could be attributed to the etching procedures. More recently, Goncharova *et al* performed a detailed study on the oxygen gettering by Ti overlayers on $HfO_2/SiO_2/Si$ structures using various analytical techniques including medium energy ion scattering (MEIS) [11]. They also observed slight oxygen depletion in HfO_2 with a 5-nm-thick Ti layer by the in-situ MEIS observation.

5.4 Conclusions

High-resolution RBS was used to study the oxygen-gettering by a titanium overlayer on $HfO_2/SiO_2/Si(001)$ structure. After titanium deposition at room temperature, oxygen is released from the SiO_2 layer into the Ti layer and the thickness of the SiO_2 layer is reduced by ~ 0.2 nm. Upon annealing the $Ti/ HfO_2/SiO_2/Si(001)$ at 330 °C in UHV, further reduction of the SiO_2 layer occurs. In addition, oxygen is also released from the HfO_2 layer after annealing when the Ti layer is thicker.

5.5 Acknowledgement

We are grateful to Drs. Kazuyoshi Torii, Satoru Kamiyama and Yasuo Nara for providing the $HfO_2/SiO_2/Si(001)$ samples. This work was partially supported by NEDO. This work was also supported by the Center of Excellence for Research and Education on Complex Function Mechanical System (COE program) of the Ministry of Education, Culture, Sports, Science and Technology.

References

[1] G. Lucovsky, Y. Wu, H. Niimi, V. Misra, and, J. C. Philips, Appl. Phys. Lett. **74**, 2005 (1999).

[2] A. Fissel, H. J. Osten, and, E. Bugiel, J. Vac. Sci. Technol. B **21**, 1765 (2003).

[3] G. D. Wilk, R.M. Wallace, and, J.M. Anthony, J. Appl. Phys. **89**, 5243 (2001).

[4] A.Callegari, E. Cartier, M. Gribelyuk, H. F. Okom-Schmidt, and T. Zabel, J. Appl. Phys. **90**, 6466 (2001).

[5] M. Copel, E. Cartier, and T. M. Ross, Appl. Phys. Lett. **78**, 1607 (2001).

[6] H. Kim, P.C. McIntyre, C.O. Chui, K.C. Saraswat, and S. Stemmer, J. Appl. Phys. **96**, 3467 (2004).

[7] S. Kamiyama, T. Miura, and Y. Nara, Appl. Phys. Lett. **87**, 132904 (2005).

[8] K. Kimura, S. Joumori, Y. Oota, K. Nakajima and M. Suzuki, Nucl. Instr. and Methods B, **219-220**, 351(2004).

[9] M. Hansen, Constitution of Binary Alloys (McGraw-Hill, New York 1958), p. 1069.

[10] K.-I. Seo, D.-I. Lee, P. Pianetta, H. Kim, K.C. Saraswat, and P.C. McIntyre, Appl. Phys. Lett. **89**, 142912 (2006).

[11] L. V. Goncharova, M. Dalponte, T. Gustafsson, O. Celik, E. Garfunkel, P. S. Lysaght, and G. Berauker, J. Vac. Sci. Technol. A **25**, 261 (2007).

Chapter 6

The development of the Time-of-flight RBS

Abstract

A new time-of-flight (TOF) RBS system is developed for application on thin film analysis. A 2-dimensional position-sensitive and time-resolving detector which contains micro channel plates (MCP) and two delay-line anodes allows 3-dimentional quantitative and nondestructive analysis with a reasonable depth resolution. The observed energy resolution of this TOF-RBS system with 100 keV He^+ ion is 2.78 keV, and the typical depth resolution is 70 Å for Si. The developed TOF-RBS is applied to crystallographic analysis of Si(100). Clear blocking patterns were observed. The results reveal that TOF-RBS using a large solid angle detector is promising for crystallographic analysis of thin films.

6.1 Introduction

With the down scaling of microelectronic devices, higher quality surface processing technologies and more precise analysis methods are required [1]. Rutherford backscattering spectroscopy (RBS) is one of the most promising surface analysis methods for such requirement [2]. The simple Rutherford cross section formula guarantees a high accuracy in composition analysis. The precision of the tabulated stopping power allows accurate depth profiling [3]. For the analysis of the crystallographic information, channeling and/or blocking techniques can be used. The high-resolution RBS (HRBS) system described in the Section 2.2, however, is not a suitable system for the blocking measurement, because it does not provide angular distributions of scattered ions.

Using the TOF detector system, a new HRBS system (referred to as TOF-RBS), which is capable to measure angular and energy distributions simultaneously, was developed for the analysis of the crystallographic information of the surface area of the sample. The TOF-RBS system employed a pulsed He^+ ion beam for an incident beam. The projectiles scattered by atoms in the sample are detected by a 2-dementional delay-line-detector (2D-DLD). The detector consists of two delay-line anodes wound perpendicularly to each other. TOF-RBS spectroscopy provides 3-dimentional information; on the spatially 2-dimentional angular distribution of particles scatted from a sample and, as the third dimensional information, on flight times of scattered particles. Energies of scattered particles are evaluated from the flight time analysis.

In the case of a small solid angle detector, the sample and/or detector setting angle must be changed several times even for the single surface analysis for the blocking measurement, since the blocking patterns over the wide range of scattering angle are necessary. However, by using a large solid angle detector in TOF-RBS, a blocking pattern over a wide scattering angle range can be obtained at the single setting of experimental geometry [4, 5] and a precise structural analysis can be carried out with a small error. There is an additional advantage of this TOF-RBS over the conventional HRBS. While the conventional RBS cannot measure neutral particles, TOF-RBS can measure all particles irrespective of charge states. This guarantees more precise quantitative analysis. Thus, TOF-RBS equipped with a large solid angle detector is greatly advantageous.

In this chapter, the development of a TOF-RBS system equipment with a 2D-DLD (RoentDek, DLD120) of 120 mm is reported. The performance of the developed

TOF-RBS system was examined by measuring a Si(001) sample.

6.2 Experimental

6.2.1 Equipments

The setup of the TOF-RBS system has been introduced in Section 2.5. We will give a brief description here. The TOF-RBS system consists of four major components: a 400 kV accelerator, a beam chopping system, a scattering chamber and a 2D-DLD. Figure 2-7 gives the schematic drawing of the whole system. We used 100 keV He^+ ions as a probe.

The 2D-DLD could identify the position and the arriving time of a particle which is recorded as a successful event by time-to-digital-converter (TDC). Therefore, this new TOF-RBS system can provide both the energy spectrum and the angular distribution of the scattered ions simultaneously.

6.2.2 Estimation of the width of the pulsed beam

The schematic drawing of the chopping system is shown in Fig. 6-1(a). The chopping system consists of a pulse generator, two electric field plates (electrostatic deflector) which are parallel to the ion beam, an entrance slit and an exit slit which are perpendicular to the ion beam. Only the electric field plates and the slits are shown in Fig. 6-1(a). The width of the entrance slit d_1 (A_1B_1) is 1 mm and the width of the exit slit d_2 (A_4B_4) is 0.6 mm as shown in Fig. 6-1(a). The distance, L, between the exit of the deflector and the exit slit is 1570 mm. The length of the electric field plates l is 30 mm and they are separated by distance d_0 of 4.25 mm. One of the plates is grounded and the other plate is applied high voltage bipolar pulses which are generated by the pulse generator. The shape of the pulse is shown in Fig. 2-8. The pulse height V_0 can be as high as 450 V and the frequency can be changed from 50 Hz up to 500 kHz. If the ion travels through the deflector during the applied voltage is $+V_0$ ($-V_0$), the ion deflected rightward (leftward) and cannot pass through the exit slit. If the voltage changes from $-V_0$ ($+V_0$) to $+V_0$ ($-V_0$) at a proper timing, the ion can pass through the exit slit. An example of the trajectory of the ion which passes through the exit slit is shown by a red curve in Fig. 6-1(a).

Let us consider the trajectory of the ion when the applied voltage changes from $-V_0$ to $+V_0$ during the passage through the deflector at $t = T$. The origin of time axis ($t = 0$) is defined by the time when the ion arrives at the entrance of the deflector. The x

position of the ion at the exit slit is given by

$$x_4 = \frac{qeE}{M_1} \cdot \left[\frac{T_0}{2}(2T + 2\tau - T_0) - \frac{\tau^2}{3} + T_L(2T - T_0 + \tau) \right] + x_1, \qquad (6\text{-}1)$$

where x_1 is the x position at the entrance of the deflector, M_1 is the projectile mass, E represents the electric field in the deflector, τ represents the rising time of the leading edge of the pulse, T_L represents the time interval for the ion flying from the exit of the deflector to the exit slit. The calculated x_4 for $x_1 = 0$ is shown as a function of T by a solid line in Fig. 6-1(c). When $|x_4| < d_2/2$, the ion can go through the chopping system. If the width of the entrance slit is infinitesimally small ($d_1 = 0$), the time spread, Δt, of the pulsed beam can be given by

$$\Delta t = \frac{d_2}{(T_0 + 2T_L) \cdot \frac{qeE}{M_1}}. \qquad (6\text{-}2a)$$

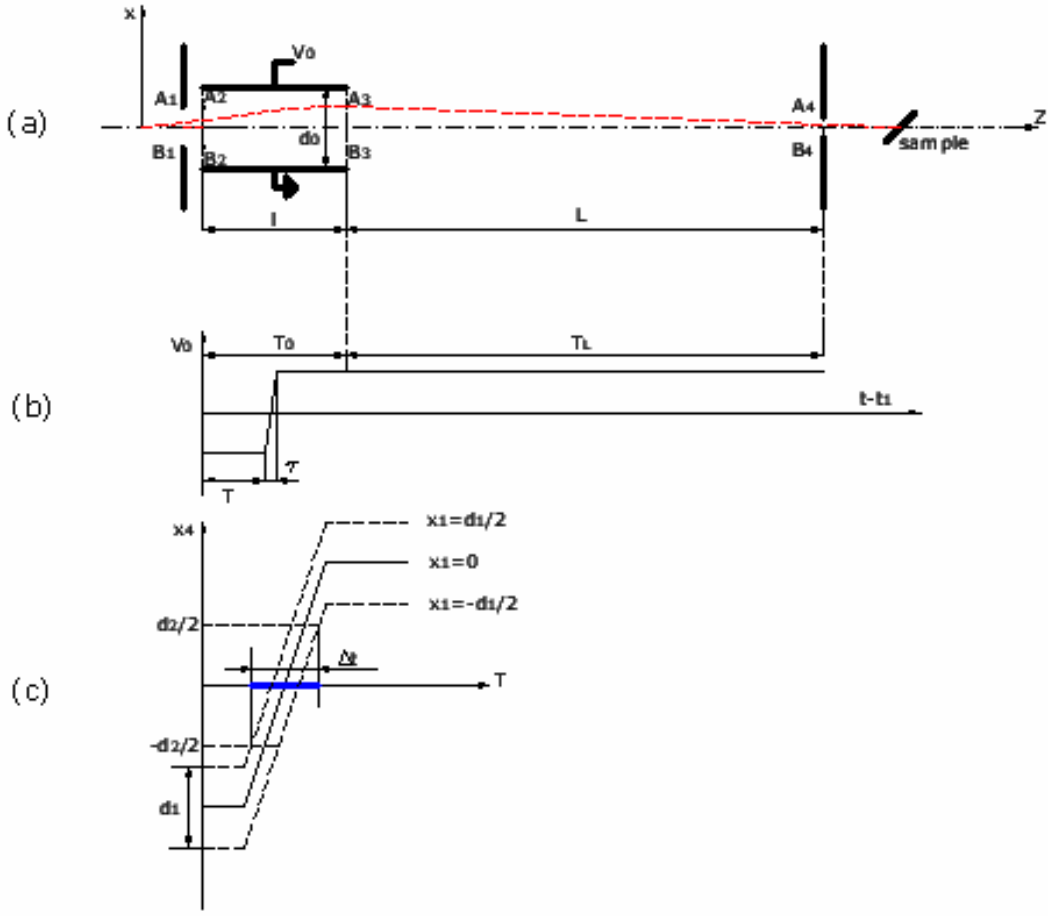

Fig. 6-1 Schematic drawing of chopping system of TOF-RBS system.

If $x_1 \neq 0$, the ion can pass through the exit slit at different T. The calculated x_4 for $x_1 = \pm d_1/2$ are also shown by dashed lines in Fig. 6-1(c). Thus the total time spread is given by

$$\Delta t = \frac{d_1 + d_2}{(T_0 + 2T_L) \cdot \dfrac{qeE}{M_1}}, \tag{6-2b}$$

which is shown by a blue line in Fig. 6-1(c). The time spread for the present chopping system is estimated to be 0.524 ns.

There is an additional time spread in this chopping system. Let us consider the case shown in Fig. 6-1(a), i.e. the applied voltage changes from $-V_0$ to $+V_0$ during passage of the ion through the deflector. The ion is accelerated by the applied voltage upon entrance slit to the deflector. The energy gain by this acceleration is given by,

$$e \cdot \Delta V = e \cdot \left(\frac{d_0/2 + x_2}{d_0} \cdot V_0 \right), \tag{6-3a}$$

where x_2 is the x position at the entrance of the deflector. During the ion traveling through the deflector the applied voltage is changed from $-V_0$ to $+V_0$. Therefore, the ion is accelerated again upon exit from the deflector. The energy gain by this acceleration is given by,

$$e \cdot \Delta V = -e \cdot \left(\frac{d_0/2 + x_3}{d_0} \cdot (-V_0) \right), \tag{6-3b}$$

where x_3 is the x position at the exit of the deflector. Because $x_3 \approx x_2$ ($= x_1$), the total energy gain is given by,

$$\Delta E_{gain} = 2e \cdot \left(\frac{d_0/2 + x_1}{d_0} \cdot V_0 \right). \tag{6-4a}$$

If the pulsed beam is generated when the applied voltage changes from $+V_0$ to $-V_0$ during passage of the ion through the deflector, the ion is decelerated and the energy loss is given by,

$$\Delta E_{loss} = 2e \cdot \left(\frac{d_0/2 + x_1}{d_0} \cdot V_0 \right). \tag{6-4b}$$

Thus the total energy spread caused by the chopping system becomes,

$$\Delta E = 2eV_0 \cdot \left(1 + \frac{d_1}{d_0} \right). \tag{6-4c}$$

In the present system with $V_0 = 375$ V, the total energy spread is estimated to be 926 eV.

This energy spread causes the time spread of the pulsed beam δt_{energy} = 3.71 ns. Including the time spread induced by the geometry of the chopping system (0.52 ns), the overall time width of the beam pulse is estimated to be 4.23 ns.

If we choose only the beam pulses produced at the rising edge of the high voltage pulse, the energy spread can be reduced as,

$$\Delta E = 2eV_0 \frac{d_1}{d_0}. \tag{6-5}$$

In the present system with V_0 = 375 V, the energy spread and corresponding time spread are estimated to be 176 eV and 0.69 ns, respectively. The overall time width of the beam pulse is, then, estimated to be 1.21 ns in this case.

Since we measure the ion flying time by TOF system to estimate its energy, all the time spread contribute to the energy resolution.

In this work, beam pulses produced at both the rising and falling edges of the high voltage pulses were used.

6.2.3 Derivation of the depth information

The data that PC can read from TDC is four-fold raw date: x1, x2, y1, y2, which correspond to the time intervals between the timing signal from the pulse generator and the signals from the delay-line anodes. This raw data can be converted into position and timing information by:

$$\begin{aligned} x &= (x1 - x2) \cdot C_x, \\ y &= (y1 - y2) \cdot C_y, \\ t &= \frac{x1 + x2}{2} \cdot C_t, \end{aligned} \tag{6-6}$$

where C_x, C_y and C_t are the conversion coefficients, x and y are the detecting position of the ions on the 2D-DLD, and t is the arriving time of the ions on the 2D-DLD.

Figure 6-2 shows the scattering geometry of the TOF-RBS experiment. The beam pulse arrives the target at time t_0 and the scattered particles arrive the 2D-DLD at time t, the energy of the particle has the expression as:

$$E_{out} = \frac{M_1}{2} \frac{d^2 + x^2 + y^2}{(t - t_0)^2}. \tag{6-7}$$

The scattering angle θ and exit angle β can be estimated from the detecting position,

$$\cos\theta = \frac{-x}{\sqrt{x^2 + y^2 + d^2}}, \tag{6-8}$$

$$\cos\beta = \frac{x\cos\alpha + d\sin\alpha}{\sqrt{x^2 + y^2 + d^2}}, \tag{6-9}$$

where α is the angle of incidence.

According to the introduction in Section 2.1.1, the depth D at which projectiles are scattered is estimated by:

$$D = \frac{K(\theta)E_0 - E_{out}}{\left(\frac{K(\theta)}{\cos\alpha}\frac{dE}{dx}\Big|_{E_0} + \frac{1}{\cos\beta}\frac{dE}{dx}\Big|_{K(\theta)E_0}\right)}, \tag{6-10}$$

where $K(\theta)$ is the kinematic factor at the scattering angle of θ, E_0 the incident energy of the He^+ before entering the sample, $(dE/dx)|_{E0}$ and $(dE/dx)|_{K(\theta)E0}$ the stopping powers in the inward path and outward path, respectively.

The depth resolution at the surface is given by:

$$\delta D = \frac{\delta E}{[S]}, \tag{6-11}$$

where δE is the energy resolution, $[S]$ the energy loss factor. Since $[S]$ has dependence

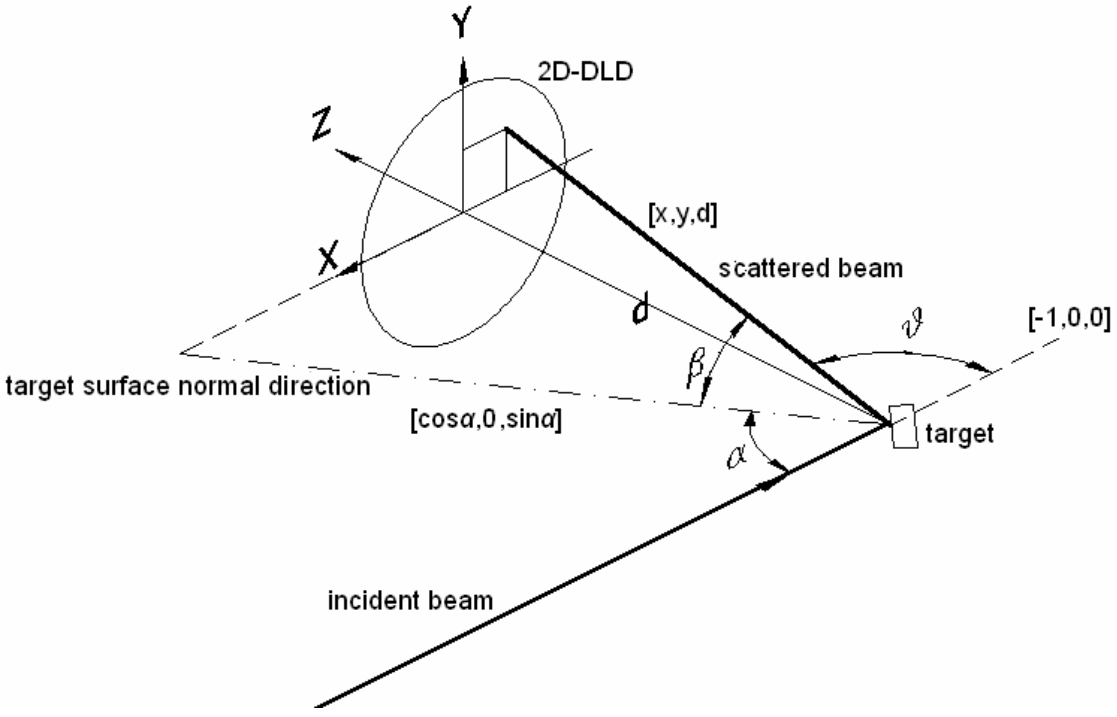

Fig. 6-2 The experimental geometry of TOF-RBS analysis.

on the scattering geometry such as θ, the depth resolution depends on the position of the detection.

In the present TOF-RBS system with 100 keV He^+, the width of the pulsed beam is 4.23 ns as was estimated in Section 6.2.2. This causes the energy resolution δE_{in} = 2.43 keV in the present system (d = 50 cm). The time resolution of the detector system is 0.15 ns which induces the energy resolution δE_d of 0.15 keV in the present system. Assuming that these contributions are independent, the overall energy resolution is given by:

$$\delta E = \sqrt{\delta E_{in}^2 + \delta E_d^2} = 2.43 \qquad keV \,. \tag{6-12}$$

Using Eqs. (6-11) and (6-12) the depth resolution around the center area ($x = 0$, $y = 0$) of the detector is estimated to be 49 Å for Si surface.

6.3 Results

6.3.1 Determination of t_0

An example of the observed TOF spectrum for the ions detected in the center region of the detector, $(x^2+y^2)^{1/2} < 5$ mm, was shown in Fig. 6-3. The sharp peak at ~840 ns corresponds to the photons emitted upon ion impact onto the target. The stretched peak extending from ~1100 ns to ~2000 ns represents the He^+ ions scattered from Si. The leading edge of the Si signal is at 1102 ns. Since we cannot precisely measure the distance between the sample and the detector d, the leading edge difference between the photon and the He^+ scattered from surface Si atoms could help to estimate d more precisely, which is 506 mm. Besides, the time that the ions arriving on the sample, t_0, also could be estimated to be 836 ns from the photon signal. Using the obtained t_0, the flight time can be estimated by $t - t_0$.

6.3.2 The energy spectra and depth profiles

The energy spectrum was derived from the detected ions in the whole area of the 2D-DLD when 100 keV He ions were incident on Si sample. The derived energy spectrum is shown by a black curve in Fig. 6-4. The energy resolution estimated from the leading edge is 4.43 keV, which is much larger than the calculated energy resolution (2.43 keV) in Section 6.2.3. This is because the scattering angle θ strongly depends on the detected position, especially x, as can be seen from Eq. (6-8). Thus the energy of the leading edge also depends on x. Due to this kinematic broadening effect, the

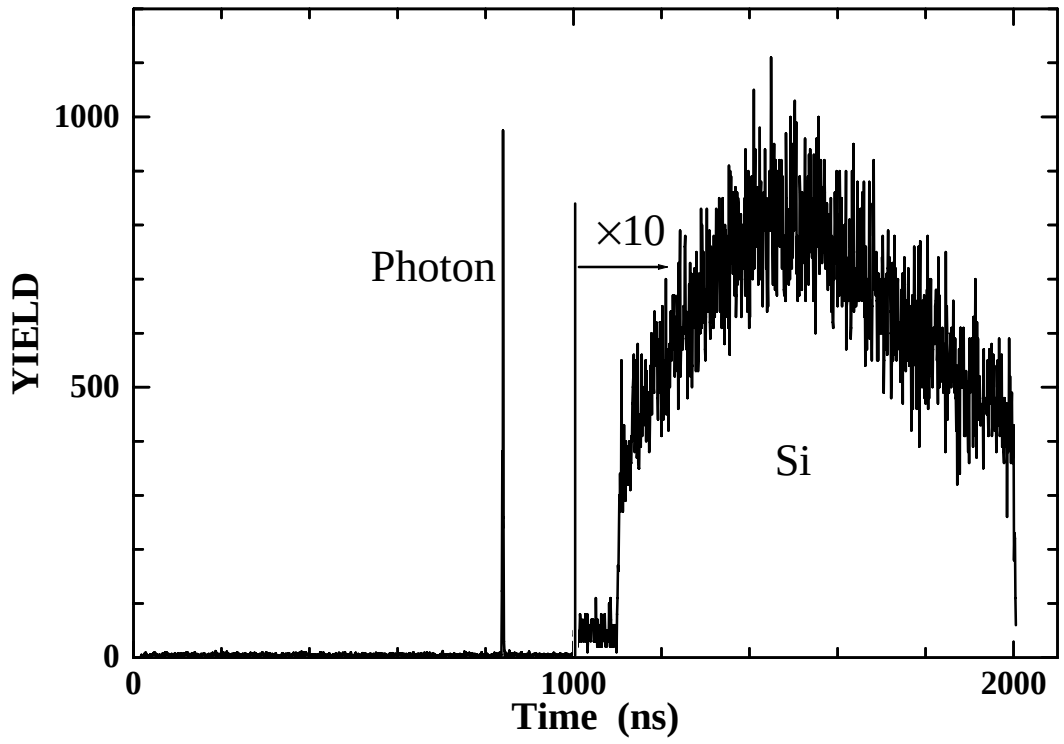

Fig. 6-3 The TOF spectrum of Si(100) for the ions detected in the region $(x^2+y^2)^{1/2} < 5$ mm.

leading edge becomes broader and the apparent energy resolution is larger than the real energy resolution. In order to clarify the influence of the kinematic broadening the detection area was divided into 6 strips, -60 mm < x < -40 mm, -40 mm < x < -20 mm, -20 mm < x < 0 mm, 0 mm < x < 20 mm, 20 mm < x < 40 mm, and 40 mm < x < 60 mm. The energy spectra of the ions detected in these strip areas are shown in Fig. 6-4. All the energy spectra were normalized by the yield to clarify the leading edge difference. The energy of the leading edge decreases with increasing x, showing the effect of the kinematic broadening. The separation between the adjacent spectra is ~0.8 keV, which is in good agreement with the energy difference, 0.82 – 0.87 keV, estimated from Eq. (2-1). Thus the kinematic broadening for the spectrum of single strip is estimated to be ~0.8 keV, while the apparent energy resolution estimated from the width of leading edge is 3.56 keV. Assuming that the kinematic broadening causes rectangular shape broadening (this is a good approximation for the central strips), the real energy resolution can be estimated by de-convolution procedure. The obtained energy resolution is 2.78 keV, which is in good agreement with the calculated resolution (2.43 keV).

Now we will derive depth spectrum from the observed data. In the conventional HRBS, Eq. (6-10) with a constant θ can be used to convert the energy into the depth because the acceptance angle is small. In the present TOF-RBS, however, the acceptance angle is so large that the effect of the scattering angle difference cannot be neglected in the conversion from energy spectrum into the depth profile. It is necessary to precisely estimate θ and β for each detected particle using Eqs. (6-8) and (6-9) in order to obtain a better depth resolution. Using Eq. (6-10) and the estimated θ and β, the depth from which the particle is scattered could be calculated. The converted depth profile of Si is shown in Fig. 6-5. The depth resolution under current experimental condition is estimated to be 70 Å.

6.3.3 Observation of the blocking pattern

The TOF-RBS image showing the blocking patterns of He^+ particles which are scattered from the depth of 50-500 Å is shown in Fig. 6-6. The color table at the right of Fig. 6-6 indicates the number of counts per pixel. The range of the scattering angle θ is 90 ± 6.85 ° with the experimental geometry. Since the position resolution of the MCP is less than 0.1 mm, the angular resolution of the TOF-RBS system at a distance of 506 mm is less than 0.01 °. This angular resolution is sufficient to examine the details of the observed blocking patterns.

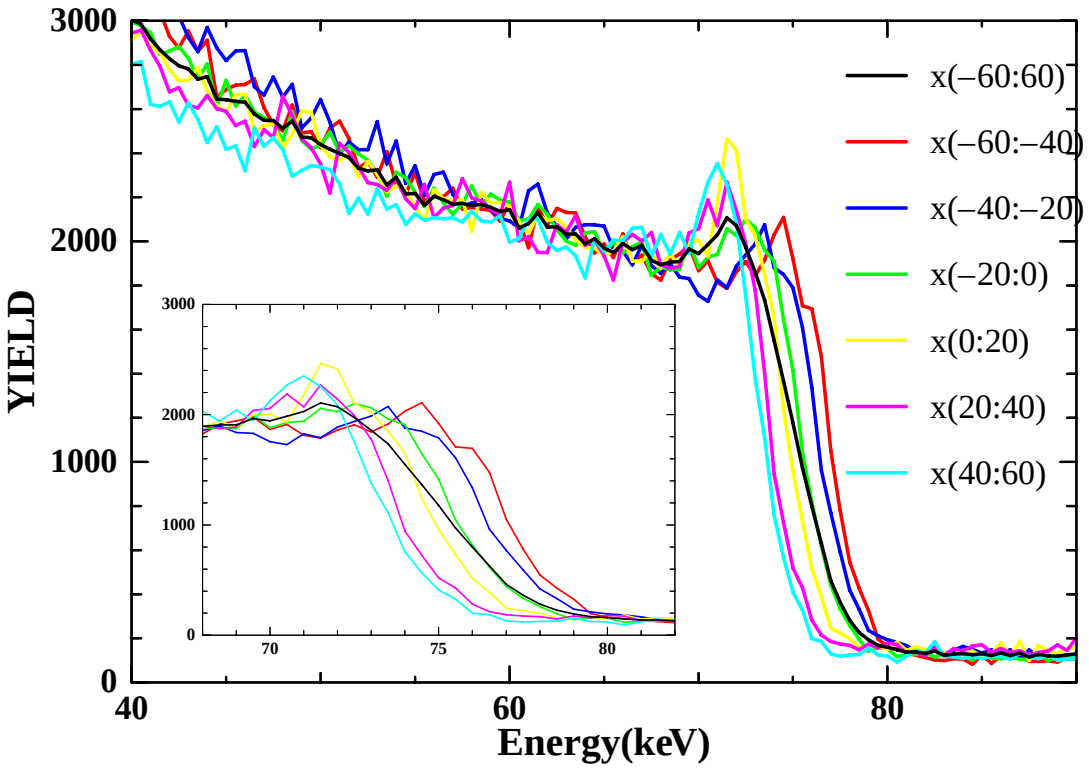

Fig. 6-4 The energy spectrum of Si(100) observed by TOF-RBS system within -60 mm < x < 60 mm (black line), -60 mm < x < -40 mm (red line), -40 mm < x < -20 mm (blue line), -20 mm < x < 0 mm (green line), 0 mm < x < 20 mm (yellow line), 20 mm < x < 40 mm (purple line), and 40 mm < x < 60 mm (cyan line). The sub-figure is the enlarged leading edge area.

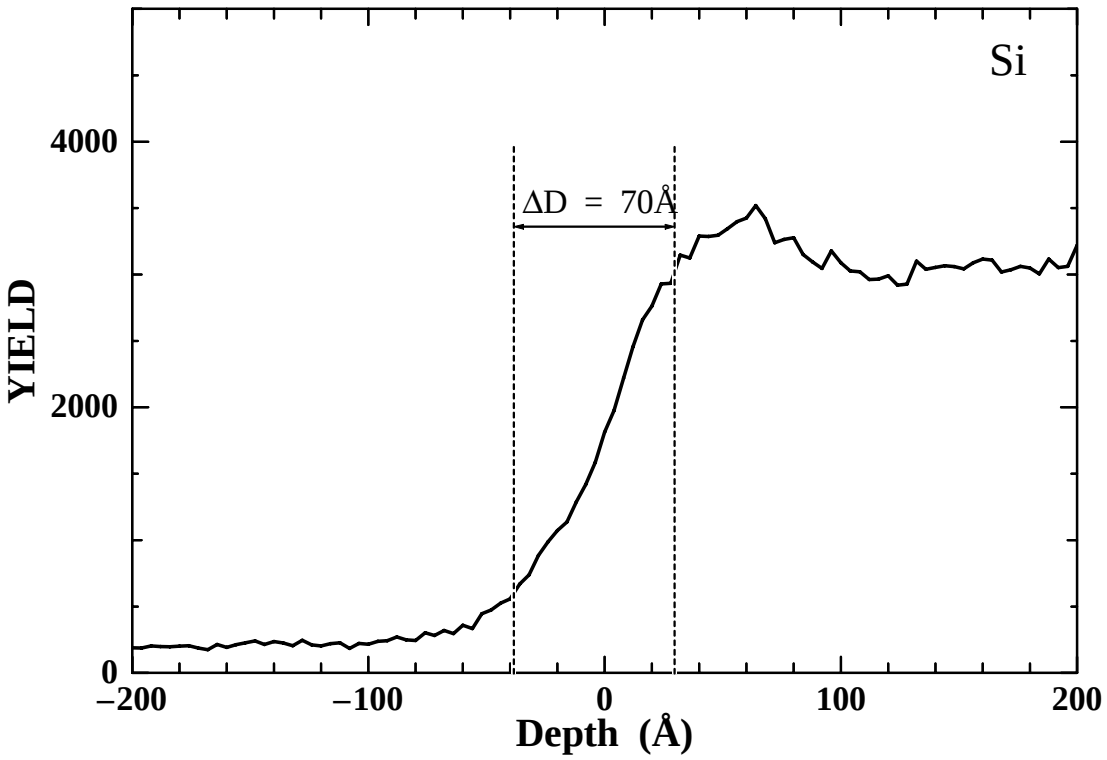

Fig. 6-5 Depth profile of the Si(100) measured by TOF-RBS.

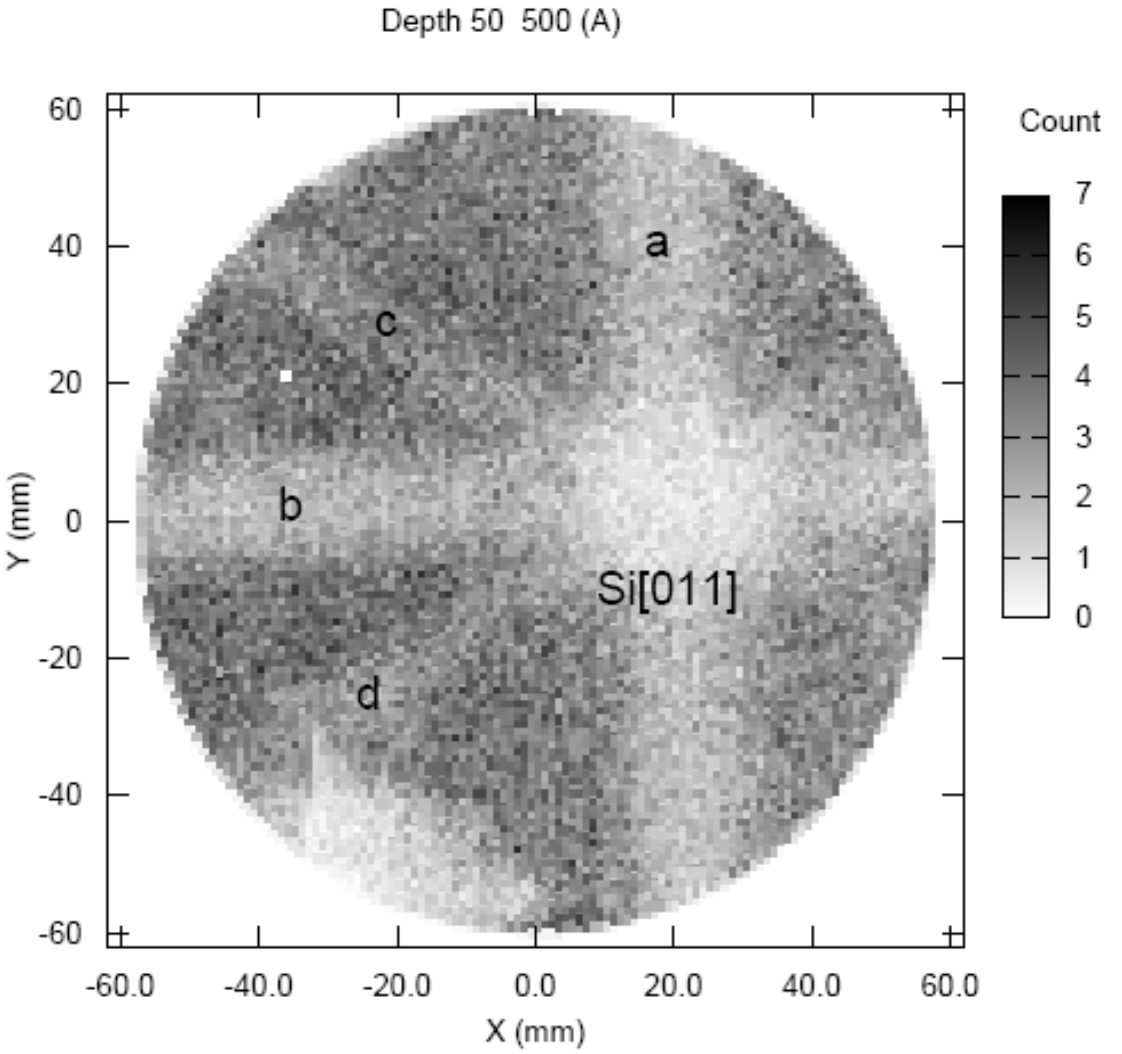

Fig. 6-6 The TOF-RBS image showing the blocking patterns of He^{+} particles scattered from the sample Si(001), where the sampling depth is 50-500 Å. The blocking pattern originated by Si[011] axis is observed. The blocking patterns labeled by a, b, c, and d are indexed to the directions of Si(100), Si$(0\bar{1}1)$, Si$(1\bar{1}1)$ and $(\bar{1}\bar{1}1)$, respectively. A low yield area caused by the low efficiency area of the MCP appears at the left-lower corner of the image.

A clear circular blocking pattern is observed at x = 20 mm, y = 0 mm. It is originated from the blocking effect of Si[011] axis. Four belt-like blocking patterns are observed. The belt-like blocking patterns labeled by a, b, c, and d are caused by the blocking effect of the atomic planes of Si(100) and $(01\bar{1})$, $(1\bar{1}1)$ and $(\bar{1}\bar{1}1)$, respectively. The results reveal that TOF-RBS using a large solid angle detector is promising for crystallographic analysis.

A low yield area at x = -20 mm, y = -50 mm is observed. This is not due to a real shadow pattern. It is caused by the low efficiency area of the MCP. If the bias voltage applied to the MCP front was increased, this shadowed area will become pale, but cannot be entirely eliminated.

6.3.4 Depth dependence of the blocking pattern

In order to investigate the dependence of the blocking pattern on the depth at which projectiles are scattered by atoms in the sample, TOF-RBS images are observed by changing the sampling depth. Observed depth region is divided into 6 parts. Figure 6-7 shows the results; (a) the depth of 0-300 Å, (b) the depth of 300-600 Å, (c) the depth of 600-900 Å, (d) the depth of 900-1200 Å, (e) the depth of 1200-1500 Å, (f) the depth of 1500-1800 Å.

The blocking patterns from the shallower regions (Fig. 6-7(a) and (b)) show clear Si[011] blocking patterns. However, the blocking patterns in Fig. 6-7(c) and 6-7(d) seem to be smoothed out. The blocking patterns of the higher index patterns (Si$(11\bar{1})$ and $(\bar{1}\bar{1}1)$) diminish when the depth is larger than 600 Å. The blocking patterns disappeared completely when the depth at which the projectiles are scattered is larger than 1200 Å. The particles scattered at a deeper depth suffer intense multiple scattering during the outgoing from the scattered position. As the result, the blocking patterns produced by high index axes and planes become unclear with increasing depth. The low yield belt-area observed at y = 20 mm in Fig. 6-7(e) is not due to the real blocking patterns. It is also a fault of MCP (low efficient area) and can be observed in Fig. 6-7(c) and 6-7(d), too. In Fig. 6-7(f), the left side of the image is blank due to the larger energy loss in this area, which means the particles scattered at the depth deeper than 1500 Å on this direction cannot arrive in the time window of the TDC.

6.4 Conclusions

The TOF-RBS system has been developed for crystallographic structure analysis of

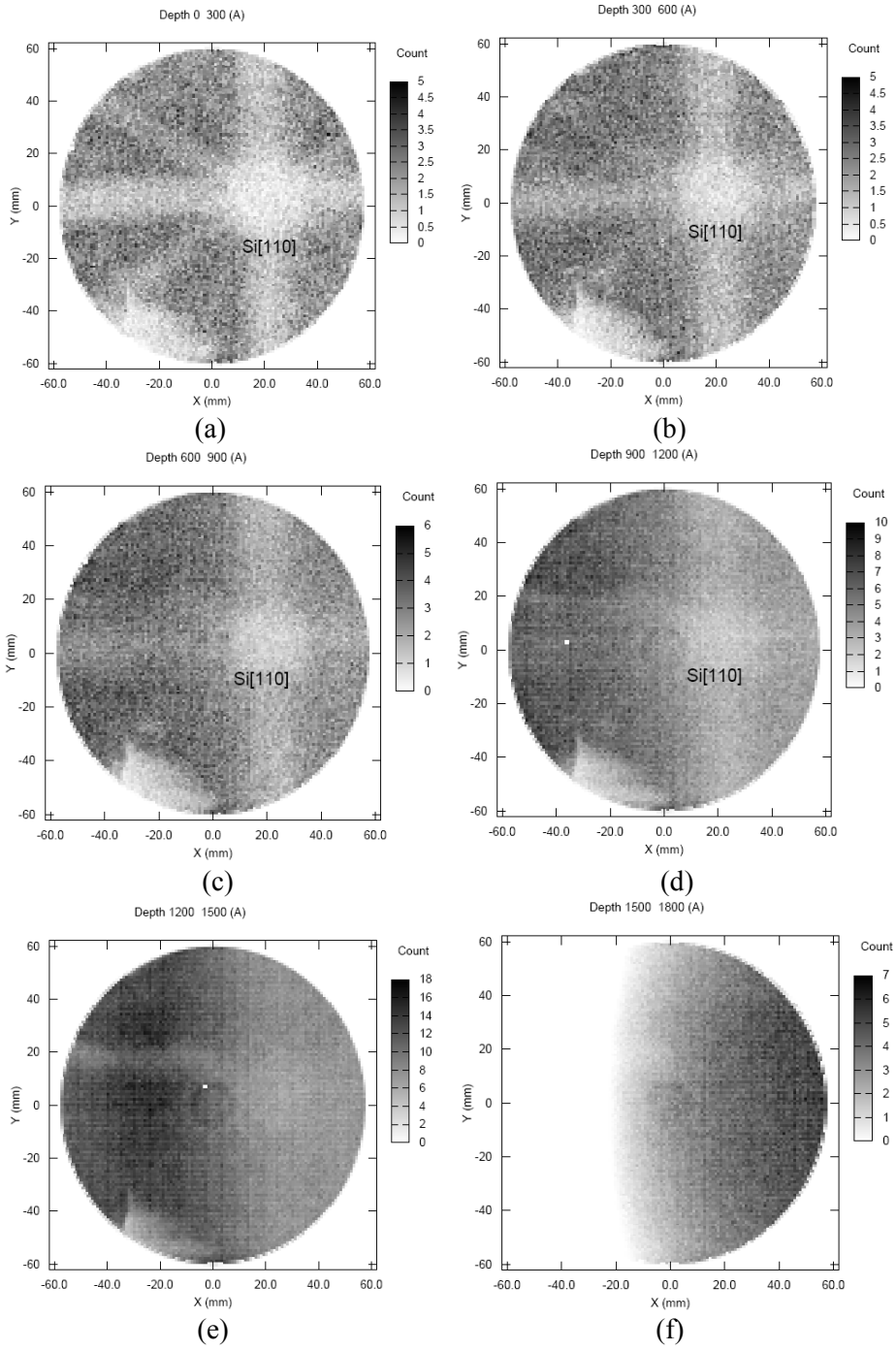

Fig. 6-7 Sampling depth dependence of the TOF-RBS image, where the depth is (a) 0-300 Å, (b) 300-600 Å, (c) 600-900 Å, (d) 900-1200 Å, (e) 1200-1500 Å, (f) 1500-1800 Å. The images obtained by the sampling at the shallower depth show clear blocking patterns. However, the blocking patterns cannot be observed clearly when the depth deeper than 900 Å.

materials. Pulsed He^+ ion beam at 100 keV incident upon a Si(100) epitaxial sample, and scattered particles are detected by a position-sensitive and time-resolving MCP detector with two delay-line anodes. The blocking pattern originated by the Si[011] axes was clearly observed. Moreover, the four belt-like blocking patterns from atomic planes of Si(100) and $(0\bar{1}1)$, $(1\bar{1}1)$ and $(\bar{1}\bar{1}1)$, were observed, which indicates that the TOF-RBS performs well for crystallographic structure analysis of materials. The energy resolution and depth resolution of TOF-RBS system is estimated to be 2.78 keV and 70 Å, respectively from the observed spectrum.

Reference

[1] C.F. McConville, T.C.Q. Noakes, S. Sugden, P.K. Hucknell, C.J. Sofield, Nucl. Instrum. Methods. Phys. Res. B **118**, 573 (1996).

[2] K. Kimura, S. Joumori, Y. Oota, K. Nakajima, M. Suzuki, Nucl. Instrum. Methods Phys. Res. B **219-220**, 351 (2004).

[3] E. Bøgh, Phys. Rev. Lett, **19**, 61 (1967).

[4] T. Kobayashi, Nucl. Instrum. Methods Phys. Res. B **249**, 266 (2006).

[5] S. Shimoda, T.Kobayashi, J. Appl. Phys. **96**, 3550 (2004).

List of publications

Journal Paper

Publications concerning this thesis

1) *Si emission from the SiO_2/Si interface during the growth of SiO_2 in the HfO_2/SiO_2/Si structure*
Zhao Ming, Kaoru Nakajima, Motofumi Suzuki, Kenji Kimura, Masashi Uematsu, Kazuyoshi Torii, Satoshi Kamiyama, Yasuo Nara, Keisaku Yamada
Appl. Phys. Lett. **88**,153516 (2006)

2) *An isotopic labeling study of the oxygen diffusion in HfO_2/SiO_2/Si*
Zhao Ming, Kaoru Nakajima, Motofumi Suzuki, Kenji Kimura, Masashi Uematsu, Kazuyoshi Torii, Satoshi Kamiyama, Yasuo Nara, Heiji Watanabe, Kenji Shiraishi, Toyohiro Chikyow, Keisaku Yamada
Appl. Phys. Lett. **90**, 133510 (2007)
selected for the April 9, 2007 issue of Virtual Journal of Nanoscale Science & Technology.

3) *In situ observation of oxygen gettering by Titanium overlayer on HfO_2/SiO_2/Si using high-resolution Rutherford backscattering spectroscopy*
Kaoru Nakajima, Akira Fujiyoshi, Zhao Ming, Motofumi Suzuki, Kenji Kimura
J. Appl. Phys. **102,** 064507 (2007)

Publications concerning other studies:

1) *Influence of Annealing Temperature on the Structure and Surface Morphology of Titanium Oxide Thin Film*
Hou Yaqi, Zhuang Daming, Zhang Gong, Zhao Ming, Wu Minsheng
Vacuum Science and Technology **22**, 247 （2002)

2) *DDVP Potocatalytic degradation of TiO_2 Film Grown by Mid-frequency Reactive Magnetron Sputtering*
Zhao Ming, Zhuang Daming, Zhang Gong, Fang Ling, Wu Minsheng Liu Jiajun
Vacuum Science and Technology **23**, 132 (2003)

3) *Influence of Annealing Temperature on the Properties of Titanium Oxide Thin Film*
Ya-Qi Hou, Da-Ming Zhuang, Gong Zhang, Ming Zhao, Min-Sheng Wu
Applied Surface Science **218**, 98 (2003)

4) *Substrate Temperature Dependence of the Properties of ZAO Thin Films Deposited by Magnetron Sputtering*
Fu En-Gang, Zhuang Da-Ming, Zhang Gong, Yang Wei-Fang, Zhao Ming
Applied Surface Science **217**, 88 (2003).

5) *A Study on the Preparation of $TiO_{2-x}N_x$ Films by Reactive Deposition and Their Absorption Properties in Visible Region*
Zhao Ming, Zhuang Daming, Zhang Gong, Fang Ling, Wu Minsheng
Chinese Journal of Materials Research **18**, 108 (2004)

6) *Effects of Cu-In precursor film phase structure on $CuInSe_2$ film properties*
Fang Ling, Zhang Gong, Zhuang Daming, Zhao Ming, Zheng Qilin, Ding Xiaofeng, Wu Minsheng
Journal of Tsinghua University **44**, 1096 (2004)

7) *Effects of composition segregation in Cu-In precursor films on microstructures of CIS films*
Fang Ling, Zhang Gong, Zhuang Daming, Zhao Ming, Zheng Qilin, Ding Xiaofeng, Wu Minsheng
Journal of Tsinghua University, **44**, 593 (2004)

8) *A Study on the Preparation of $TiO_{2-x}N_x$ Films by Reactive Deposition and Their Absorption Properties in Visible Region*
Zhao Ming, Zhuang Da-Ming, Zhang Gong, Fang Ling
Materials Science Forum **475-479**, 1223 (2005)

9) *Combination of high-resolution RBS and angle-resolved XPS: Accurate depth profiling of chemical states*
Kenji Kimura, Kaoru Nakajima, Ming Zhao, Hiroshi Nohira, Takeo Hattori, Masaaki Kobata, Eiji Ikenaga, Jung Jin Kim, Keisuke Kobayashi, Thierry Conard, Wilfried Vandervorest
Surfac and Interface Analysis, *in press*.

International Conference

1] *High-resolution Rutherford Backscattering Spectroscopy for Nano-CMOS applications*
Kenji Kimura, Zhao Ming, Kaoru Nakajima, Motofumi Suzuki
International Workshop on Nano CMOS
Jan 30 – Feb. 1, 2006, Mishima, Japan

2] *High-resolution RBS analysis of Si-dielectrics interfaces*
Zhao Ming, Kaoru Nakajima, Motofumi Suzuki, Kenji Kimura, Masashi Uematsu, Kazuyoshi Torii, Satoshi Kamiyama, Yasuo Nara, Heiji Watanabe, Kenji Shiraishi, Toyohiro Chikyow, Keisaku Yamada,
2006 International Conference on Solid State Devices and Materials
September 13-15, 2006, Yokohama, Japan
Extended Abstract Book, p380-381.

3] *Oxidation process of $HfO_2/SiO_2/Si$ structures observed by high-resolution RBS*
Zhao Ming, Kaoru Nakajima, Motofumi Suzuki, Kenji Kimura, Masashi Uematsu, Kazuyoshi Torii, Satoshi Kamiyama, Yasuo Nara, Heiji Watanabe, Kenji Shiraishi, Toyohiro Chikyow, Keisaku Yamada,
The 8th International Conference on Solid-State and Integrated-Circuit Technology
Oct. 23-26, 2006, Shanghai, China
Proceedings of The 8th International Conference on Solid-State and Integrated-Circuit

Technology, p. 392 – 395.

4] *Interface Reaction of High-k Gate Stack Structures Observed by High-resolution RBS*
Zhao Ming, Kaoru Nakajima, Motofumi Suzuki, Kenji Kimura Masashi Uematsu2, Kazuyoshi Torii, Satoshi Kamiyama, Yasuo Nara, Heiji Watanabe, Kenji Shiraishi, Toyohiro Chikyow, Keisaku Yamada
The 212th ECS meeting,
Oct. 7 – 12, 2007, Wahinton, DC, USA
ECS Transactions, vol. 11 No. 4 (2007) pp.103-115.